Icarus 326 (2019) 133–150

Contents lists available at ScienceDirect

Icarus

journal homepage: www.elsevier.com/locate/icarus

Near-Earth asteroid 2012 TC4 observing campaign: Results from a global planetary defense exercise

Vishnu Reddy[a,*], Michael S. Kelley[b], Davide Farnocchia[c], William H. Ryan[d], Cristina A. Thomas[e], Lance A.M. Benner[c], Jessie Dotson[f], Marco Micheli[g], Melissa J. Brucker[a], Schelte J. Bus[h], Marina Brozovic[c], Lorien Wheeler[i], Viqar Abbasi[j], James M. Bauer[k], Amber Bonsall[l], Zarah L. Brown[a], Michael W. Busch[m], Paul Chodas[c], Young-Jun Choi[n,o], Nicolas Erasmus[p], Kelly E. Fast[b], John P. Faucher[q], Rachel B. Fernandes[a], Frank D. Ghigo[l], David G. Gilbank[p], Jon D. Giorgini[c], Annika Gustafsson[e], Olivier Hainaut[r], Walter M. Harris[a], Joseph S. Jao[c], Lindley S. Johnson[b], Theodore Kareta[a], Myung-Jin Kim[n], Detlef Koschny[s], Emily A. Kramer[c], Rob R. Landis[b], Denis G. Laurin[j], Jeffrey A. Larsen[q], Clement G. Lee[c], Cassandra Lejoly[a], Tim Lister[t], Robert McMillan[a], Joseph R. Masiero[c], Donovan Mathias[u], Michael Mommert[v], Hong-Kyu Moon[w], Nicholas A. Moskovitz[x], Shantanu P. Naidu[c], Ravi Teja Nallapu[y], Haris Khan Niazi[z], John W. Noonan[a], David Polishook[aa], Eileen V. Ryan[d], Lauren Schatz[ab], James V. Scotti[a], Benjamin Sharkey[a], Boris M. Shustov[ac], Amanda A. Sickafoose[p,ad], Marc A. Silva[ae], Martin A. Slade[c], Lindsay R. Slick[a], Lawrence G. Snedeker[ae], Alessondra Springmann[a], David Tholen[af], David E. Trilling[e,p], Alberto Q. Vodniza[ag], Richard Wainscoat[af], Robert Weryk[af], Makoto Yoshikawa[ah]

[a] Lunar and Planetary Laboratory, University of Arizona, 1629 E University Blvd, Tucson, AZ 85721, USA
[b] Planetary Defense Coordination Office, Planetary Science Division, NASA Headquarters, 300 E St SW, Washington, DC 20546, USA
[c] Jet Propulsion Laboratory, California Institute of Technology, 4800 Oak Grove Drive, Pasadena, CA 91109, USA
[d] Magdalena Ridge Observatory, New Mexico Tech, 801 Leroy Place, Socorro, NM 87801, USA
[e] Dept. of Physics and Astronomy, Northern Arizona University, PO Box 6010, Flagstaff, AZ 86011, USA
[f] NASA Ames Research Center, MS 245-6, Moffett Field, CA 94035, USA
[g] ESA SSA-NEO Coordination Centre, Largo Galileo Galilei, 1, 00044 Frascati, RM, Italy
[h] Institute for Astronomy, University of Hawaii, 2860 Woodlawn Drive, Honolulu, HI 96822-1839, USA
[i] RedLine Performance Solutions/CSRA, NASA Ames Research Center, MS 258-6, Moffett Field, CA 94035, USA
[j] Canadian Space Agency, John H Chapman Space Centre, 6767 route de l'aeroport, St-Hubert, J3Y 8Y9 Ottawa, Canada
[k] Department of Astronomy, University of Maryland, College Park, MD 20742, USA
[l] Green Bank Observatory, Green Bank, WV 24944, USA
[m] SETI Institute, Mountain View, CA 94043, USA
[n] Korea Astronomy and Space Science Institute 776, Daedeokdae-ro, Yuseong-gu, Daejeon 34055, Republic of Korea
[o] University of Science and Technology 217, Gajeong-ro, Yuseong-gu, Daejeon 34113, Republic of Korea
[p] South African Astronomical Observatory, Cape Town, 7925, South Africa
[q] US Naval Academy, 121 Blake Rd, Annapolis, MD 21402, USA
[r] European Southern Observatory, Karl-Schwarzschild-Straße 2, 85748 Garching bei München, Germany
[s] ESTEC, European Space Agency, Keplerlaan 1, 2200, AG, Noordwijk, the Netherlands
[t] Las Cumbres Observatory, 6740 Cortona Drive, Goleta, CA 93117, USA
[u] NASA Ames Research Center, MS 258-5, Moffett Field, CA 94035, USA
[v] Lowell Observatory, 1400 W. Mars Hill Road, Flagstaff, AZ 86001, USA
[w] Korea Astronomy and Space Science Institute, 776, Daedeokdae-ro, Yuseong-gu, Daejeon 34055, Republic of Korea
[x] Lowell Observatory, 1400 West Mars Hill Road, Flagstaff, AZ 86001, USA
[y] Dept. of Aerospace and Mechanical Engineering, University of Arizona, 1130 N Mountain Ave, Tucson, AZ 85721, USA
[z] College of Optical Sciences, University of Arizona, 1630 E University Blvd, Tucson, AZ 85719, USA
[aa] Department of Earth and Planetary Science, Weizmann Institute, Herzl St 234, Rehovot 7610001, Israel
[ab] College of Optical Sciences, University of Arizona, 1629 E University Blvd, Tucson, AZ 85721, USA
[ac] Institute of Astronomy RAS, Pyatnitskaya str. 48, 119017 Moscow, Russian Federation
[ad] Department of Earth, Atmospheric, and Planetary Sciences, Massachusetts Institute of Technology, Cambridge, MA 02139-4307, USA

* Corresponding author.
E-mail address: reddy@lpl.arizona.edu (V. Reddy).

https://doi.org/10.1016/j.icarus.2019.02.018

Available online 21 February 2019

[ae] SAITECH, Goldstone Deep Space Communication Complex, Fort Irwin, CA 92310-5097, USA
[af] Institute for Astronomy, University of Hawaii, 2680 Woodlawn Drive, Honolulu, HI 96822, USA
[ag] Dept. of Physics, University of Nariño, Calle 18 - Carrera 50, Block 1, Torobajo headquarters, San Juan de Pasto, Colombia
[ah] Japan Aerospace Exploration Agency, 3-1-1 Yoshinodai, Chuo-ku, Sagamihara, Kanagawa 252-5210, Kanto, Japan

A B S T R A C T

Impacts due to near-Earth objects (NEOs) are responsible for causing some of the great mass extinctions on Earth. While nearly all NEOs of diameter > 1 km, capable of causing a global climatic disaster, have been discovered and have negligible chance of impacting in the near future, we are far from completion in our effort to detect and characterize smaller objects. In an effort to test our preparedness to respond to a potential NEO impact threat, we conducted a community-led global planetary defense exercise with support from the NASA Planetary Defense Coordination Office. The target of our exercise was 2012 TC4, the ~10 m diameter asteroid that made a close pass by the Earth on 2017 October 12 at a distance of about 50,000 km. The goal of the TC4 observing campaign was to recover, track, and characterize 2012 TC4 as a hypothetical impactor in order to exercise the global planetary defense system involving observations, modeling, prediction, and communication. We made three attempts with the Very Large Telescope (VLT) on 2017 July 27, 31 and on 2017 August 5 and recovered 2012 TC4 within its ephemeris uncertainty at 2.2 arcmin from the nominal prediction. At visual magnitude V = 27, the recovery of 2012 TC4 is the faintest NEA detection thus far. If an impact during the 2017 close approach had been possible based on the 2012 astrometric data, these recovery observations would have been sufficient to confirm or rule out the impact. The first automatic detection by a survey (Pan-STARRS1) was on September 25, which is the earliest that 2012 TC4 would have been discovered in survey mode, if it had not been discovered in 2012. We characterized 2012 TC4 using photometry, spectroscopy and radar techniques. Based on photometric observations, we determined a rotation period of 12.2 min with an amplitude of 0.9 magnitudes. An additional lower amplitude period was detected, indicating that 2012 TC4 was in a state of non-principal axis rotation. The combined visible and near-infrared spectrum puts it in the taxonomic X-class. Radar images at 1.875 m resolution placed only a few range pixels on the asteroid, reveal an angular, asymmetric, and elongated shape, and establish that 2012 TC4 is less than 20 m on its long axis. We estimate a circular polarization ratio of 0.57 + -0.08 that is relatively high among NEAs observed to date by radar. We also performed a probabilistic impact risk assessment exercise for hypothetical impactors based on the 2012 TC4 observing campaign. This exercise was performed as part of ongoing efforts to advance effective impact risk models and assessment processes for planetary defense. The 2012 TC4 close approach provided a valuable opportunity to test the application of these methods using realistically evolving observational data to define the modeling inputs. To this end, risk assessments were calculated at several epochs before and during the close approach, incorporating new information about 2012 TC4 as it became available. Two size ranges were assessed—one smaller size range (H = 26.7) similar to the actual 2012 TC4, and one larger size range (H = 21.9) to produce a greater-damage scenario for risk assessment. Across the epochs, we found that only irons caused significant damage for smaller size. For the larger size case, however, hydrous stones caused the greatest damage, anhydrous stones caused the least damage, and irons caused moderate damage. We note that the extent of damage depends on composition in different size regimes and, after astrometry, size is the most important physical property to determine for an incoming object.

1. Introduction

Planet Earth has survived mass extinctions, the last of which took place ~65 million years ago and led to the extinction of the dinosaurs (Alvarez et al., 1980). The impact of Comet Shoemaker-Levy 9 into Jupiter in 1994 led to the establishment of the NASA Near-Earth Object Observation (NEOO) program with the goal of discovering 90% of near-Earth Objects (NEOs) larger than 1 km. This goal has been largely accomplished and we are currently pursuing the goal of discovering 90% of NEOs larger than 140 m. More recently, the 20 m asteroid that airburst over Chelyabinsk, Russia, injuring over 1000 people and damaging thousands of buildings, only reinforced the importance of detecting and characterizing small NEAs that have a greater chance of impacting on more imminent timescales. While nearly all extinction-scale NEOs (> 1 km diameter) have been discovered with negligible chance of impacting in the near future, the best defense against the NEO threat is detecting hazardous NEOs with sufficient lead-time to divert them. In 2016, the NASA Planetary Defense Coordination Office (PDCO) was established to ensure the early detection, tracking, and characterization of potentially hazardous objects (PHOs) and to issue warnings about potential impacts. The PDCO also is the lead office for providing timely and accurate communications and coordination of U.S. Government planning for response to an actual impact threat. In an effort to test the operational readiness of all entities critical to planetary defense, we conducted a community-led exercise with support from the NASA PDCO. The target of this exercise was 2012 TC4, a ~10-meter diameter asteroid that made a close pass by the Earth on 2017 October 12 at a distance of about 50,000 km. The goal of the TC4 observing campaign was to recover, track, and characterize 2012 TC4 as a hypothetical impactor in order to exercise the global planetary defense system involving observations, modeling, predictions, and communications. Here we present an overview of the campaign and summarize the science results from the exercise.

2. Astrometry

Near-Earth asteroid 2012 TC4 was discovered by the Pan-STARRS1 survey on 2012 October 04 (MPEC 2012-T18, 2012). 2012 TC4 was in the nighttime sky within 20° of opposition and was headed for an inbound close approach to Earth on 2012 October 12 at a geocentric distance of 95,000 km (15 Earth radii). As 2012 TC4 got closer to Earth and brighter in the sky, astronomers collected hundreds of observations with the last astrometric position on 2012 October 11 at 18:00 UTC reported to the Minor Planet Center by the Drebach Observatory, Germany. After that close approach, 2012 TC4 moved into the daytime sky thus preventing further observations.

The 2012 close approach significantly changed the orbit of 2012 TC4. For instance, the semimajor axis increased from 1.3 to 1.4 AU and the orbital period changed from 1.45 to 1.67 yr. As a result, 2012 TC4 moved into a 5:3 resonance with the Earth, leading to a second encounter on 2017 October 12, which took place after five orbital revolutions of the Earth and three orbital revolutions of the asteroid.

Based on the 2012 observational dataset, the circumstances of the 2017 encounter were largely uncertain. The 3-σ uncertainty for the time of close approach was 00:48 Barycentric Dynamical Time (TDB) to 16:10 TDB and the 3-σ uncertainty for the geocentric close approach distance was 13,000 km (2 Earth radii) to 290,000 km (45 Earth radii). Fig. 1 shows the mapping on the Öpik B-plane (Kizner, 1961, Valsecchi et al. 2003) of 200 Monte Carlo samples for the orbital solution computed by using only the observations collected during the 2012 apparition. The coordinates on the B-plane represent the asymptotic relative position of the asteroid with respect to the Earth before the Earth's gravity starts bending the asteroid's trajectory. The orbital uncertainty is on a line and the Monte Carlo samples line up along the vertical direction, which is directly related to the position of the sample along the orbit and therefore to the time of close approach. This line does not intersect the Earth's cross-section on the B-plane and so an impact in 2017 was not possible based on the 2012 astrometric data.

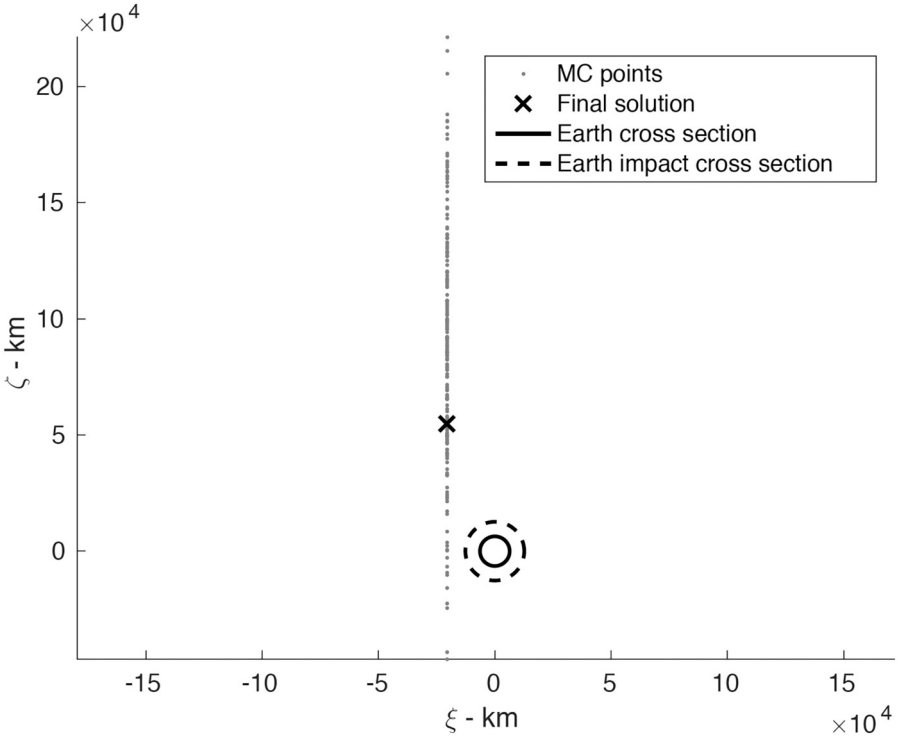

Fig. 1. B-plane for the October 2017 Earth encounter of 2012 TC4. The 200 Monte Carlo points are randomly generated from JPL orbit solution 26, which only uses astrometric data from the 2012 apparition. The final solution (marked by X) corresponds to JPL orbit solution 61, which is the reconstruction of the final trajectory. The impact cross section of the Earth is scaled from the Earth radius to account for gravitational focusing.

3. Recovery

The first opportunity to recover 2012 TC4 occurred during July 2017, more than two months before the closest approach on October 12. Fig. 2 shows the plane-of-sky uncertainty and the brightness of 2012 TC4 as seen from Earth from the beginning of July 2017 to the October 12 encounter. During this time frame, 2012 TC4 became progressively brighter and the plane-of-sky uncertainty grew larger. To minimize the area of the sky to be searched, the recovery attempt had to be performed as early as possible. Therefore, we scheduled observations with European Southern Observatory's Very Large Telescope (VLT) on Cerro Paranal, Chile, which is capable of detections as faint as V ~ 27 (Micheli et al., 2016).

To support the recovery attempts and refine the ephemeris estimate, we reanalyzed the 2012 observational data. We remeasured the astrometry that had been collected from Mauna Kea, Magdalena Ridge Observatory, Las Cumbres Observatory, Bisei Observatory, Konkoly Observatory, and Drebach Observatory. To reduce star catalog systematic errors, we performed the astrometric reduction by using the first data release of the Gaia star catalog (Gaia Collaboration et al., 2016). The remeasurements included an assessment of the astrometric uncertainties as well as timing errors, which were especially relevant for the latest observations during the 2012 apparition when 2012 TC4 reached a plane-of-sky rate of motion of almost 2 arcsec/s.

Figs. 3 and 4 show the astrometric residuals of the observations collected during the 2012 apparition against JPL solution 61, which is

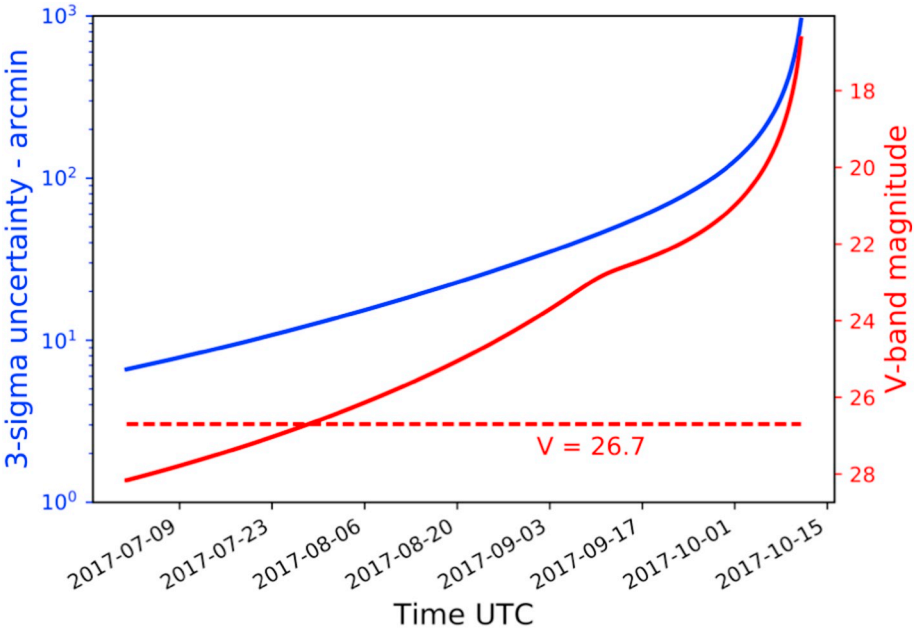

Fig. 2. The blue curve shows the semimajor axis of the 3-sigma plane-of-sky uncertainty as a function of time. The continuous red curve shows the V-band magnitude as a function of time, and the dashed red line corresponds to the faintest asteroid detection ever reported (Micheli et al., 2016). (For interpretation of the references to color in this figure legend, the reader is referred to the web version of this article.)

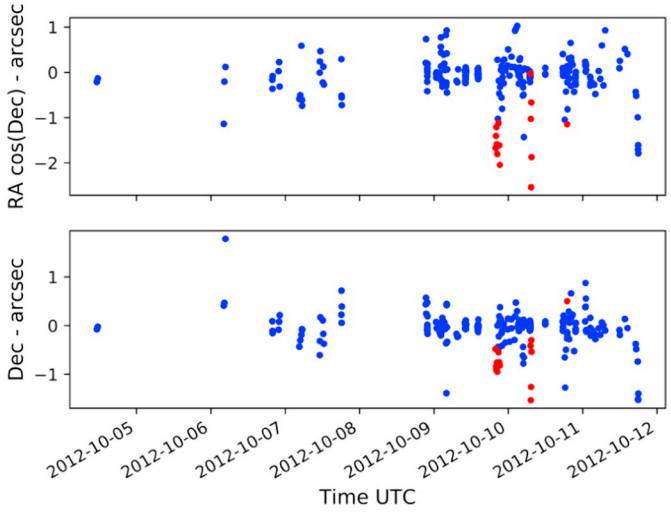

Fig. 3. Astrometric residuals of the optical observations obtained during the 2012 apparition computed against JPL solution 61. The top panel is for right ascension and the bottom panel is for declination. The right ascension residuals include the cos(declination) factor. Red dots correspond to observations excluded from the fit. (For interpretation of the references to color in this figure legend, the reader is referred to the web version of this article.)

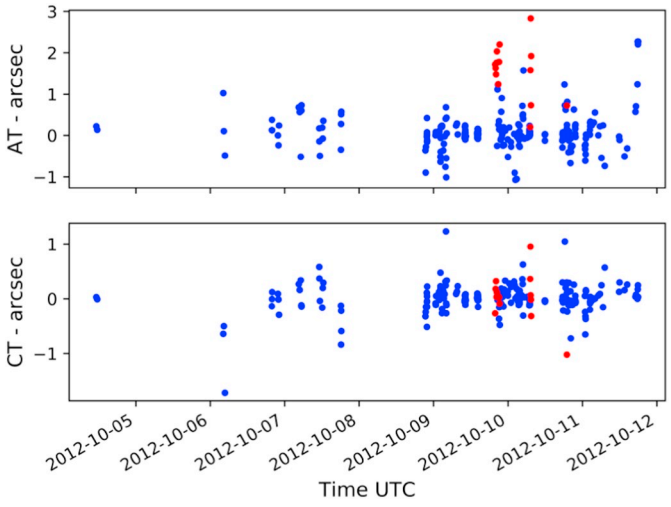

Fig. 4. Astrometric residuals of the optical observations obtained during the 2012 apparition computed against JPL solution 61. The top panel is for the along-track (AT) residuals and the bottom panel is for the cross-track (CT) residuals. Red dots correspond to observations excluded from the fit. The two panels use different scales for the y-axis. (For interpretation of the references to color in this figure legend, the reader is referred to the web version of this article.)

the final trajectory reconstruction. The residuals are represented in right ascension and declination (Fig. 3) and along-track and cross-track directions (Fig. 4). Because of their evident biases, we removed eight observations from the fit. For the observations that we reanalyzed, the data weights were set based on our astrometric uncertainty assessment. For the other observations, we adopted the Vereš et al. (2017) weighting scheme, with the exception of a few observations that we deweighted because of their higher noise level. Finally, to remove star catalog biases, we applied the Farnocchia et al. (2015a) debiasing scheme. Timing errors can significantly affect along-track residuals and in fact Fig. 4 clearly shows how the along-track residuals increase toward the end of the 2012 arc when 2012 TC4 moved faster in the sky. To mitigate the effect of timing errors, we inflated the observation uncertainties in the along-track direction to allow for a 1-second timing

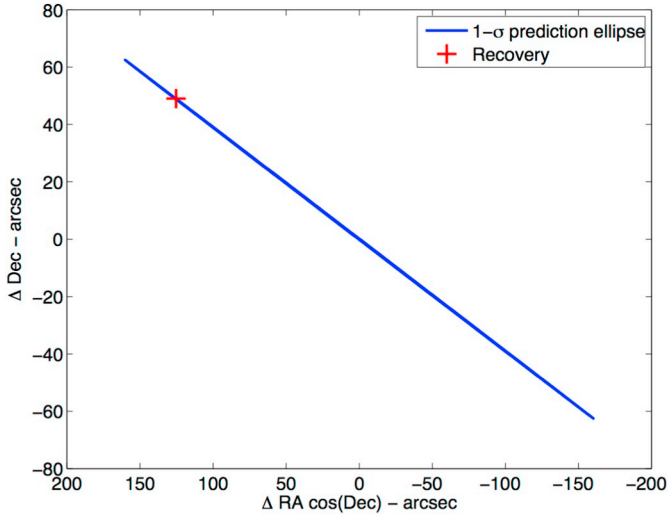

Fig. 5. Plane-of-sky prediction uncertainty of solution 26 for the first recovery detection from VLT on 2017 July 21 at 05:54 UTC. The cross marks the measured astrometric position of 2012 TC4.

error. Because of the observed along-track bias and our reanalysis of the data, the Drebach observations were further deweighted along-track for a time error of 3 s. Based on this statistical treatment of the astrometry we computed JPL orbital solution 26.

Our first recovery attempt was on 2017 July 27 and we found a candidate detection. However, the low signal-to-noise ratio of the detection cast doubt on whether we had actually detected 2012 TC4. Therefore, we observed 2012 TC4 again and successfully confirmed our candidate VLT detection with additional images taken on August 5. We also obtained a single astrometric position from a set of observations with poorer seeing on 2017 July 31. On 2017 August 6, the Minor Planet Center issued MPEC 2017-P26 to announce the recovery of the 2012 TC4. Fig. 5 shows the recovery measurement compared with the ephemeris prediction from JPL solution 26. 2012 TC4 was found 2.2 arcmin from the nominal prediction. The offset with respect to JPL solution 26 was 0.8-sigma in the longest direction of uncertainty, and the combined two-dimensional offset was 1.1-sigma.

Due to the recovery observations, the knowledge of the orbit of 2012 TC4 greatly improved. In particular, the uncertainty in semimajor axis decreased by almost three orders of magnitude. The estimated geocentric close approach distance became 50,141 ± 373 km (7.9 Earth radii) and the time of closest approach was 2017 October 12 at 05:41:59 TDB ± 67 s (3-sigma uncertainties). The new estimated orbit and the close approach circumstances made it easier to plan the subsequent astrometric and physical characterization observations. In particular, if an impact during the 2017 close approach had been possible based on the 2012 astrometric data, the recovery observations would have confirmed or ruled out the possible impact.

4. 2017 Apparition and final orbit reconstruction

After the recovery, we kept observing 2012 TC4 with the purpose of refining the orbit. By the end of August we obtained eleven astrometric positions from Mauna Kea and six from Kitt Peak. By mid-September, Magdalena Ridge and Pan-STARRS1 also observed 2012 TC4. Then, the number of observations started increasing rapidly and skyrocketed in October. In total, more than seven hundred optical observations were collected and reported to the Minor Planet Center during the 2017 apparition. We also were able to obtain observations in the days after the close approach from Magdalena Ridge and Mauna Kea observatories through October 21. Finally, we observed 2012 TC4 for the last time on 2017 December 14 from the VLT.

Table 1
Doppler measurements, uncertainties, and residuals against JPL solution 61. The measurement on Oct. 9 used DSS-14 to transmit (8560 MHz) and receive. The Doppler on Oct. 12 used DSS-12 (7190 MHz) to transmit and the Green Bank Telescope to receive.

Time UTC	Measurement (Hz)	Uncertainty (Hz)	Residual (Hz)
2017 Oct 09 07:30:00	364,428.520	1.0	−0.57
2017 Oct 12 02:21:30	278,809.719	1.0	0.19

Even though Pan-STARRS1 first detected 2012 TC4 on September 14, the detection required human intervention and a priori knowledge of the 2012 TC4 position. The first detection that was automatically reported by the Pan-STARRS1 pipeline was on September 25, which is the earliest that 2012 TC4 could have been discovered in survey mode if it had not been discovered in 2012. The September 25 Pan-STARRS1 observations alone would have provided very weak constraints on the orbit. However, with the addition of the second automatic detection from Pan-STARRS1 on September 28, JPL's Scout system (Farnocchia et al., 2015c, 2016) would have predicted the upcoming close approach and that an impact was not possible.

The close approach of 2012 TC4 represented a good opportunity to collect radar observations. In addition to providing useful information on an object's physical properties, radar measurements are very powerful for improving the orbit (Benner et al., 2015). We obtained two Doppler measurements of 2012 TC4 on October 9 and 12 (see Table 1) and seven time delay measurements on October 10, 11, and 14 (see Table 2).

Non-gravitational perturbations are important to consider for orbits of small objects such as 2012 TC4. The expected size of 2012 TC4 was between 10 and 30 m for an albedo between 5% and 30% based on the absolute magnitude of H = 26.7. Modeling these non-gravitational perturbations became important as the observation arc was extended and the orbital uncertainty shrank. We modeled non-gravitational perturbations as a purely radial component A_1/r^2 and a purely transverse component A_2/r^2, which correspond to solar radiation pressure and Yarkovsky effect respectively (e.g., Farnocchia et al., 2015b). We initially assumed a range for A_1 and A_2 based on the expected size of 2012 TC4: $A_1 = (3.0 \pm 1.5) \times 10^{-11}$ AU/d^2 and $A_2 = (0 \pm 1.5) \times 10^{-12}$ AU/d^2 (1-sigma). After the October 11 radar delay Doppler measurements, we started estimating A_1 and A_2 based on the orbital fit (Farnocchia et al., 2013).

By using the same statistical treatment of the astrometry discussed above and fitting the whole data arc, we computed our final orbit solution, JPL solution 61, which is shown in Table 3 together with our final reconstruction of the close approach. As a result of the close approach, the semimajor axis of 2012 TC4 further increased to 1.6 AU, which corresponds to an orbital period of about 2 yr. Figs. 2, 3, 6 and 7 show the astrometric residuals of optical observations against JPL solution 61. The along-track residuals clearly show large errors around the 2012 October 12 and 2017 October 12 close approaches, but especially for 2017 when the plane-of-sky rate of motion of 2012 TC4 reached almost 20 arcsec/s. Unfortunately, systematic timing errors as

Table 2
Delay measurements, uncertainties, and residuals against JPL solution 61. All measurements used DSS-14 to transmit and receive.

Time UTC	Measurement (s)	Uncertainty (μs)	Residual (μs)
2017 Oct 10 06:50:00	7.487595	20	5.3
2017 Oct 10 08:00:00	7.308629	1.0	−0.71
2017 Oct 10 08:40:00	7.2075461	0.25	−0.37
2017 Oct 11 06:10:00	3.7974858	0.25	0.28
2017 Oct 11 07:20:00	3.61681298	0.25	0.26
2017 Oct 14 12:30:00	8.7488736	0.50	0.03
2017 Oct 14 13:10:00	8.848922729	0.25	0.11

Table 3
Orbital elements, non-gravitational parameters, and close approach estimates for JPL solution 61.

	Nominal value	1-sigma uncertainty
Eccentricity	0.3360783783	2.45E-08
Perihelion distance	0.9335316890 AU	1.82E-08 AU
Time of perihelion	2017 Nov 16 00:45:42.634 TDB	0.496 s
Longitude of node	198.23273434 deg	1.04E-06 deg
Argument of perihelion	222.58388030 deg	6.98E-06 deg
Inclination	0.85717234 deg	1.05E-06 deg
A1	21.17E-12 AU/d^2	8.00E-12 AU/d^2
A2	−27.35E-14 AU/d^2	6.54E-14 AU/d^2
Close approach time	2017 Oct 12 05:41:59.633 TDB	0.003 s
Close approach distance	50,151.120 km	0.033 km

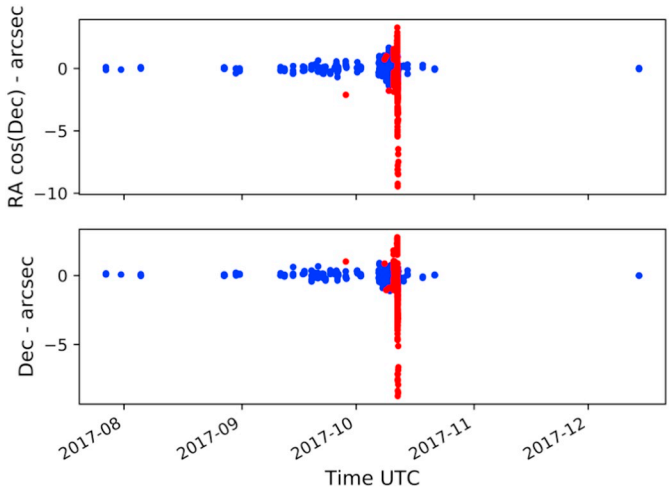

Fig. 6. Astrometric residuals of the optical observations obtained during the 2017 apparition computed against JPL solution 61. The top panel is for right ascension and the bottom panel is for declination. The right ascension residual includes the cos(declination) factor. Red dots correspond to observations excluded from the fit. (For interpretation of the references to color in this figure legend, the reader is referred to the web version of this article.)

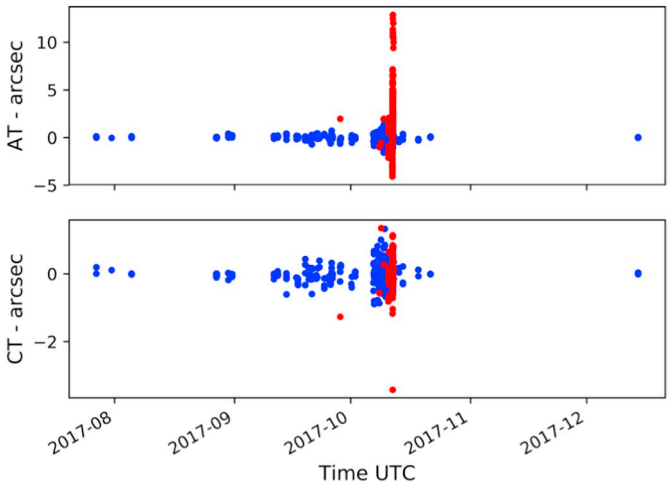

Fig. 7. Astrometric residuals of the optical observations obtained during the 2017 apparition computed against JPL solution 61. The top panel is for the along-track (AT) residuals and the bottom panel is for the cross-track (CT) residuals. Red dots correspond to observations excluded from the fit. The two panels use different scales for the y-axis. (For interpretation of the references to color in this figure legend, the reader is referred to the web version of this article.)

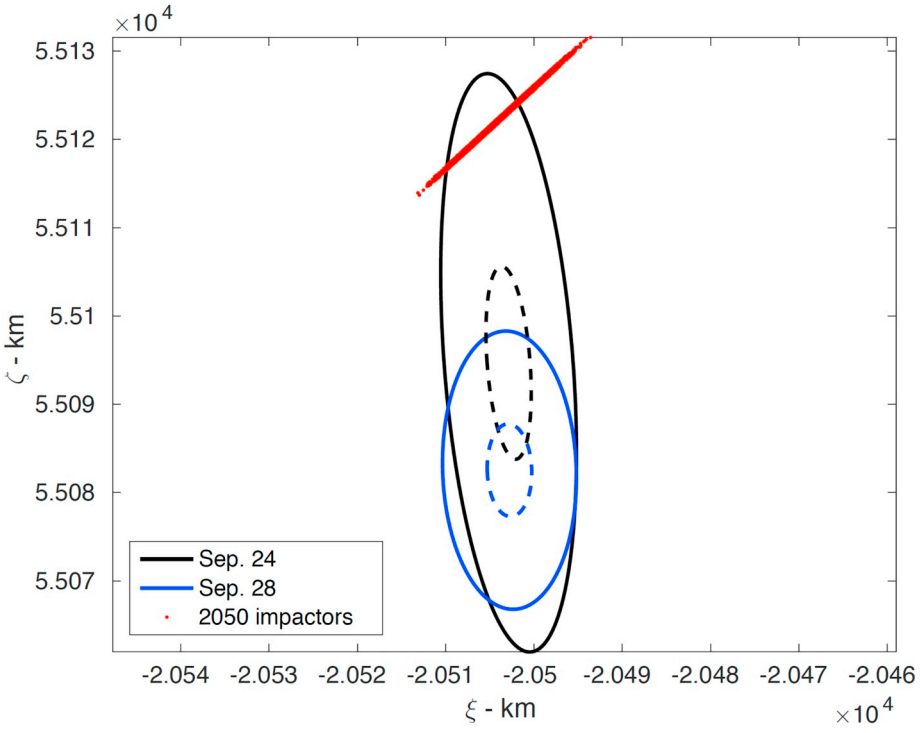

Fig. 8. Mapping on the B-plane of JPL solution 42, which had a data cutoff on 2017 September 24, and solution 46, which had a data cutoff on 2017 September 28. This B-plane is the same shown in Fig. 1, but the axes are vastly smaller because of the significantly smaller uncertainties due to the extended data arc. Solid lines are for 3-sigma uncertainty ellipses, dashed lines are for 1-sigma ellipses. The red dots correspond to impact solutions for the October 2050 Earth encounter, i.e., they identify the location of the 2050 keyhole. (For interpretation of the references to color in this figure legend, the reader is referred to the web version of this article.)

large as 5 s were present and led to the removal of the corresponding observations.

5. Virtual impactors

At the end of the 2012 apparition, 2012 TC4 was a virtual impactor with several orbital solutions compatible with the observational data that could lead to a future impact on Earth. Each of these possible impacts had a small probability of less than 5 million.

As the data were being collected during the 2017 apparition, the orbital solution started shrinking around the impact solution for October 2050. Fig. 8 shows the mapping on the B-plane corresponding to the October 2017 encounter of the orbital uncertainties for JPL solutions 42 and 46 compared with the keyhole (Chodas, 1999) for an impact in October 2050. JPL solution 42 is based on all the observations available on September 24. The uncertainty ellipse included many of the 2050 impact solutions and the impact probability was 1 in 180. On September 28, new data became available and we computed JPL solution 46. The corresponding uncertainty ellipse shrank leaving the 2050 impact solutions outside the ellipse, thus ruling out an impact in 2050. Other impact solutions remained possible for a while, but by the time the 2017 apparition concluded, the observational data had ruled out all the possible impacts for the next century.

6. Characterization: Photometry

The rotational state of a closely approaching asteroid is an essential physical parameter to acquire as part of any overall characterization effort. The spin state can reveal important information about limitations of the strength of the asteroid. Additionally, the lightcurve amplitude can lead to estimates of axial dimension ratios that in turn help approximate the shape. In the case of 2012 TC4, a 12.2 minute rotational period with a lightcurve amplitude of 0.9 magnitudes was observed during its discovery apparition in October 2012 (Polishook, 2013; Odden et al., 2013; Warner, 2013, and Carbognani, 2014). However, an additional 8.50 min period was detected during this same apparition using observations taken at a higher temporal cadence, indicating that 2012 TC4 was in a state of non-principal axis rotation (Ryan and Ryan, 2017).

Cognizant of the previous knowledge of 2012 TC4's rotation state, our international campaign to observe this asteroid in 2017 included extensive lightcurve observations as part of the exercise to assess general observational preparedness. Aside from scientific interest, this would allow for the determination of when, during its incoming trajectory, various features of 2012 TC4's lightcurve would be detectable. A complete list of facilities, telescope details, and observational circumstances for the lightcurve effort are listed in Table 4. The full data set is archived in digital format at http://2012tc4.astro.umd.edu/.

The first lightcurves were acquired using 4- to 5-meter-class telescopes in mid-September 2017 while the asteroid had a visual

Table 4
List of facilities, telescope details and observational circumstances for the lightcurve campaign. Visual magnitudes quoted are from JPL Horizons.

Observatory/Telescope	Date (UT)	Visual Mag.	Filter
Kitt Peak Mayall 4-m (USA)	2017 09 13.21–31	22.7	VR
Kitt Peak Mayall 4-m (USA)	2017 09 14.15–30	22.6	VR
Palomar Hale 5-m (USA)	2017 09 17.39–48	22.4	r
Palomar Hale 5-m (USA)	2017 09 20.15–46	22.1	r
SOAR 4.1-m (Chile)	2017 10 06.19–23	19.7	r
CTIO LCO-A 1-m (Chile)	2017 10 09.12–16	18.4	r
CTIO LCO-B 1-m (Chile)	2017 10 09.15–19	18.4	i
Magdalena Ridge 2.4-m (USA)	2017 10 09.13–22	18.4	VR
Wise Obs. 0.72-m (Israel)	2017 10 09.72–88	17.9	VR
Wise Obs. 0.72-m (Israel)	2017 10 10.67–96	16.9	VR
IRSF 1.4-m (South Africa)	2017 10 10.75–99	16.8	J,H,K
KMTNet 1.6-m (South Africa)	2017 10 10.84–98	16.7	V,R,I
USNA 0.51-m (USA)	2017 10 11.02–04	16.6	V
Magdalena Ridge 2.4-m (USA)	2017 10 11.07–16	16.4	R
Wise Obs. 0.72-m (Israel)	2017 10 11.68–82	14.7	VR
IRSF 1.4-m (South Africa)	2017 10 11.81–99	14.1	J,H,K
KMTNet 1.6-m (South Africa)	2017 10 11.83–96	14.1	V,R,I
Magdalena Ridge 2.4-m (USA)	2017 10 12.06–14	13.2	R

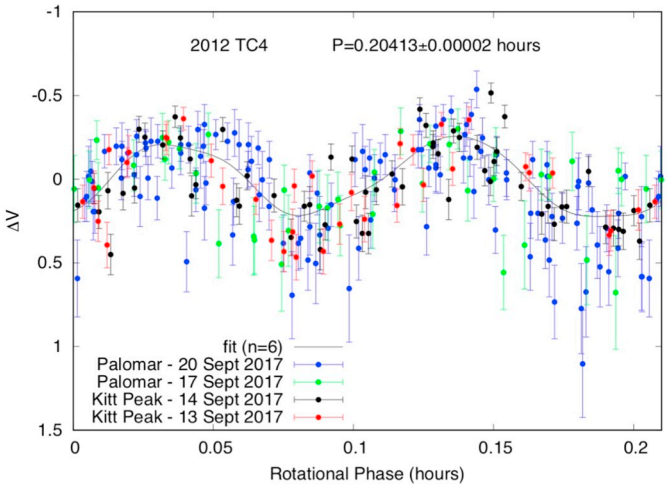

Fig. 9. Composite lightcurve showing the data acquired at both the 4-meter Mayall Telescope at KPNO and the 5-meter Hale Telescope at Palomar Observatory in mid-September 2017.

magnitude of V~22.5. The larger amplitude ~0.20 h primary period was clearly evident in these data. The composite lightcurve data folded with this single period are presented in Fig. 9. These initial data were significant to the campaign exercise in that, absent any other characterization of this object from previous apparitions, these observations would have permitted the first confirmation that 2012 TC4 was a potential impactor of non-negligible strength approximately one month before closest approach. These data also showed a spread that was larger than the photon statistics-based error bars, which was the first indication during this campaign of the possibility that a second period was present.

On 2017 October 6, 2012 TC4 was observed using the SOAR 4-meter telescope when the asteroid was at magnitude V~20.5 These data were the first to display the definitive presence of the secondary period during the 2017 observing campaign. A sequential lightcurve plot with a double Fourier series fit using periods of 0.205 h and 0.145 h is shown in Fig. 10.

Not surprisingly, the number of photometric observations by various teams increased significantly as we neared the October 12 closest approach. A composite lightcurve derived from data collected on the day before closest approach (October 11) by observers at MRO, the US Naval Academy (USNA), the Wise Observatory (Israel), and the Korean Microlensing Telescope Network (KMTNet, South Africa; Kim et al., 2016) is shown in Fig. 11. Note that in this composite plot, the Fourier fit deviates each cycle from strict periodicity due to the presence of the lower amplitude second period. The USNA data consisted of differential photometry and the MRO data was acquired using the R filter. Therefore, both were shifted vertically to align with the calibrated H(V) magnitudes (observed V scaled to unit heliocentric and geocentric distances) of the KMTNet and Wise data acquired when the asteroid was brighter. The last lightcurve data obtained during the campaign was taken about 3 h before closest approach using the MRO 2.4-m telescope on 2017 October 12.

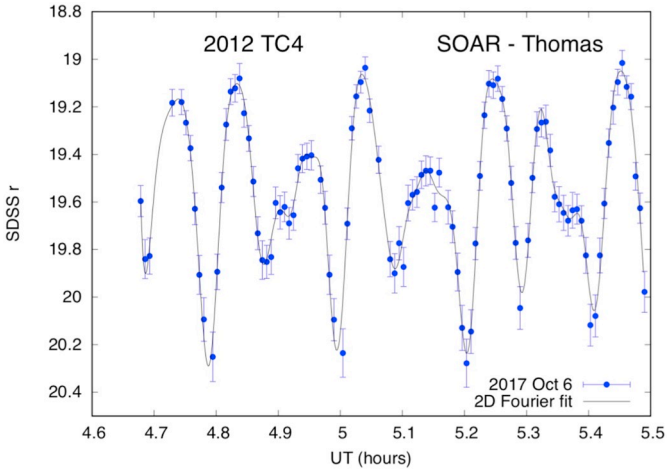

Fig. 10. Sequential lightcurve of data acquired using the SOAR 4-meter telescope fitted with a double Fourier series using periods of 0.204 h and 0.141 h.

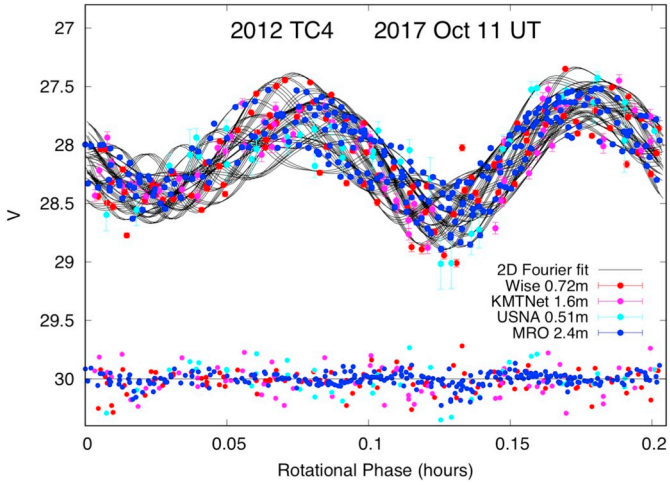

Fig. 11. Composite lightcurve using data from the US Naval Academy 0.51-meter, Magdalena Ridge Observatory 2.4-meter, the Wise Observatory 0.72-meter (Israel), and the Korean Microlensing Network's (KMTNet, South Africa) 1.6-meter telescope on 2017 October 11. Superimposed is the double Fourier series fit using the periods 0.2042 h and 0.1413 h (the best fit to the composite data) with the residuals plotted relative to V = 30. The USNA and MRO data have been adjusted in magnitude zeropoint to match the V-calibrated Wise and KMTNet data to account for different filters and the brightening of the asteroid when the latter data were acquired.

As expected, the quality of lightcurve data, both in temporal and photometric resolution, increased as the asteroid got closer (and the apparent brightness increased), making the complex character of the rotation state more evident. However, the nature of the flyby was such that the phase angle, and hence the apparent brightness, rapidly decreased after the flyby. Therefore, no lightcurves were acquired on the outgoing trajectory. Since the observing geometry was very similar to that during the discovery 2012 apparition, the characteristics of the lightcurve were very similar. In particular, the larger primary amplitude ~0.20 h and smaller secondary ~0.14 h periods seen in the 2012 data were again observed during this apparition. Warner (2018), Sonka et al. (2017) and Tan and Gao (2018) also identified similar periods. Further analysis of the data will help identify the periods to a higher precision and determine if there were any changes in the lightcurve structure or periods between the two apparitions. This additional scrutiny may also eventually permit the construction of a physical shape model of the asteroid.

7. Characterization: Colors and spectroscopy

To investigate the composition of 2012 TC4, we obtained broadband colors and visible and near-infrared spectra of the object in the weeks before closest approach. Observational circumstances for our characterization effort are shown in Table 5.

7.1. Colors

Broadband colors for this effort were obtained at four facilities: the

Table 5
List of facilities, telescope details and observational circumstances for the compositional characterization campaign. Visual magnitudes presented here are from JPL Horizons.

Observatory/telescope	Date (UT)	Visual mag.	Data type
Palomar Hale 5-m (USA)	2017 09 20.38–41	22.2	Visible Colors
Magdalena Ridge 2.4-m (USA)	2017 10 11.14–16	16.3	Visible Colors
KMTNet 1.6-m (South Africa)	2017-10-10.83-96	~16.6	Visible Colors
	2017-10-11.83-96	~13.9	
IRSF 1.4-m (South Africa)	2017-10-10.79-99	~16.6	NIR Colors
	2017-10-11.79-99	~13.7	
Lowell DCT 4.3-m (USA)	2017-10-10.14-16	17.5	Visible Spectrum
NASA IRTF 3-m (USA)	2017-10-09.35-39	18.3	NIR Spectrum

2.4-m Magdalena Ridge Observatory (MRO), the Palomar 200-inch, the 1.6-m Korea Microlensing Telescope Network (KMTNet, Sutherland node), and the 1.4-m Infrared Survey Facility (IRSF). All colors derived from our observations are consistent with a featureless, moderately sloped spectral type such as the C- or X-complex. The two independent measurements made with VRI filters (MRO and KMTNet) are consistent with each other.

7.1.1. Magdalena Ridge 2.4-m (USA)

Broadband color sequences (R-V-R-B-R-I-R) were taken during the acquisition of the R-band temporal photometry on 2017 October 11. Conditions were determined to be photometric by analyzing the comparison stars from the lightcurve data. As described in the previous section, the lightcurve was fitted with a two-dimensional Fourier series. With the temporal behavior of the lightcurve fixed, the magnitude zero point was fit to the V-, B-, and I-band data respectively. The difference in these zero points was then used to determine the instrumental color indices. The color transformation coefficients were determined using the standard field PG2213-006 (Landolt, 1992) and were checked for consistency with recent observations. The resulting color indices are listed in Table 6.

7.1.2. Palomar Hale 5-m (USA)

Colors were obtained from relative photometry using SDSS on-frame standards. The final colors are the averages of two color sequence observations taken in an rigrigr observing filter pattern and the r-band fluxes were interpolated to the approximate time of the g- and i-band exposures. Due to the relative faintness of the target on the date of observation, integration times were 360 seconds which is about half of a full rotation. The resulting color indices are listed in Table 6.

7.1.3. KMTNet 1.6-m/IRSF 1.4-m (South Africa)

Observations were performed with a node of the Korea Microlensing Telescope Network (KMTNet) and with the Infrared Survey Facility (IRSF) telescope in Sutherland, South Africa. For KMTNet, observations were performed alternating among V, R, and I filters in the sequence VRVI, repeating the sequence continuously for the entire observing duration. The exposure time for each filter on both nights was 15 s with a ~90-second read-out time in-between exposures. For IRSF, simultaneous J, H and K filter imaging was done during the entire observing duration. The exposure time for each filter was 60 and 10 s on October 10 and 11 respectively, with < 3 second read-out time between exposures.

For both KMTNet and IRSF data the photometry and lightcurve extraction was performed using PHOTOMETRYPIPELINE (PP) developed by Mommert (2017). The pipeline utilizes the widely used Source Extractor software for source identification and aperture photometry. SCAMP is used for image registration. Both image registration and photometric calibration are based on matching field stars with star catalogs from the Sloan Digital Sky Survey, the AAVSO Photometric All-Sky Survey, Pan-STARRS, and GAIA. To determine colors and to account for variations in magnitude due to rotation, a linear interpolation was performed between adjacent V data points in the KMTNet's data set. The interpolation was used to obtain a corrected V magnitude at times of non-V observations. Respective colors were derived by subtracting the non-V magnitudes from these interpolated V magnitudes. The simultaneous J, H and K imaging of IRSF did not require this additional step for color determination. The repeating sequences enabled the study of color indices over time for both nights (Table 6). No color variation within the observed errors was seen for either the visible or near-infrared wavelengths between the two nights or within a single night.

7.2. Spectroscopy

Visible and near-infrared spectra were obtained using Lowell Observatory's 4.3-m Discovery Channel Telescope (DCT) near Flagstaff, Arizona, and the 3-m NASA Infrared Telescope Facility (IRTF). Observational circumstances for the spectroscopy effort are shown in Table 5. The composite visible and near-infrared spectrum of 2012 TC4

Table 6
Broadband visible and NIR colors for 2012 TC4.

Observatory/Telescope	Date (UTC)	B-V	V-R	V-I
Magdalena Ridge 2.4-m (USA)	2017 10 11.14-16	0.64 ± 0.06	0.44 ± 0.04	0.85 ± 0.06
KMTNet 1.6-m	2017 10 10.84-98		0.351 ± 0.063	0.86 ± 0.064
(South Africa)	2017 10 11.83-96		0.480 ± 0.073	0.76 ± 0.069

Observatory/Telescope	Date (UTC)	g-r	r-i	g-i
Palomar Hale 5-m (USA)	2017 09 20.38-41	0.55 ± 0.07	0.46 ± 0.07	1.01 ± 0.08

Observatory/Telescope	Date (UTC)	J-H	J-K
IRSF 1.4-m	2017 10 10.75–99	0.324 ± 0.020	0.35 ± 0.034
(South Africa)	2017 10 11.81-99	0.33 ± 0.001	0.33 ± 0.001

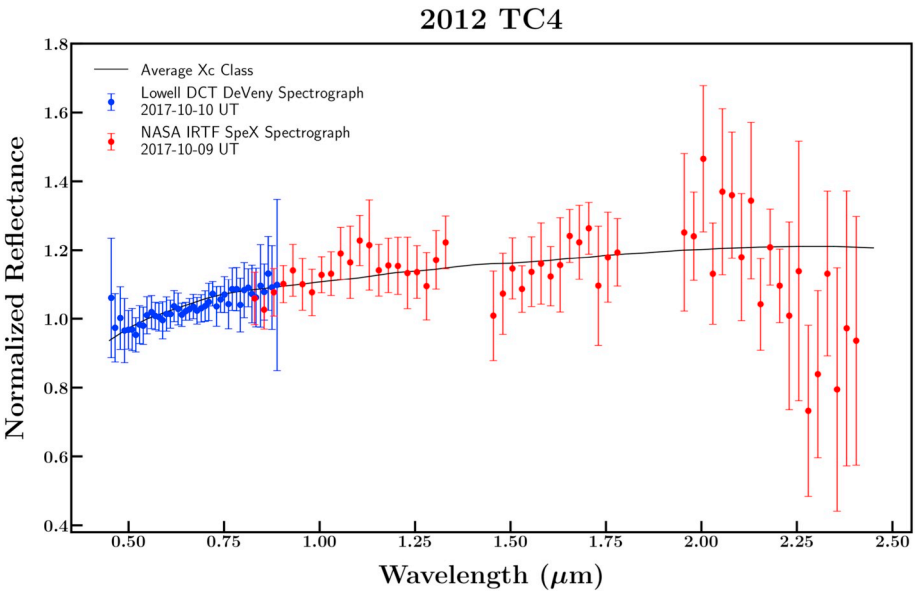

Fig. 12. Combined visible and near-infrared spectrum of 2012 TC4 along with average spectrum of Xc taxonomic type.

is shown in Fig. 12. The combined spectrum puts it in the taxonomic X-complex with a best spectral match to the Xc-class. Our spectrum is consistent with the spectrum of 2012 TC4 taken by the MITHNEOs survey during its discovery apparition (Binzel et al., 2019).

7.2.1. Lowell DCT 4.3-m (USA)

Visible wavelength spectra were obtained with the DeVeny Spectrograph at Lowell Observatory's 4.3 m Discovery Channel Telescope on the night of 2017 October 10 UT. DeVeny was configured with a 150 line/mm grating and a 3 arcsec wide slit, producing a usable free spectral range of approximately 4500–9000 Å and a dispersion of 4.3 Å per pixel. Under high winds and poor seeing of 4–5 arcsec, six exposures of 300 s were obtained for a total of 30 min on source. Solar analog star SA115–271 was observed immediately after 2012 TC4. A combination of four arc lamps (Hg, Cd, Ne, Ar) and a flat field lamp were independently measured at the pointing location of the asteroid to provide a dispersion solution and flat field correction respectively. Reduction of these data followed Moskovitz et al. (2013) and used standard IRAF and IDL procedures.

7.2.2. NASA IRTF 3-m (USA)

Near-infrared spectra were obtained with SpeX (Rayner et al., 2003) on the NASA Infrared Telescope Facility (IRTF) on 2017 October 9. The spectra were taken in prism mode with the 0.8 arcsec wide slit. The sky conditions were poor, with moderate to thick cirrus that thinned out long enough to obtain 1800 s of total integration on the target. The solar analog star SA 115-271 was also observed. The data were wavelength calibrated using an internal Ar lamp. The spectrum shows no sign of a thermal tail out to 2.4 μm. While the formal errors and scatter in the K-band region are large, a thermal signature would have been detected if it were present.

The spectral properties of 2012 TC4 are consistent with an optically bright object. This conclusion agrees with the radar analysis, which finds that the object is likely an E-type (the optically bright sub-type of the X-complex). While a wide range of taxonomic types (E, M, and P-types representing high, moderate and low albedo groups) are present within the X-complex, the lack of a thermal tail past 2.2 μm in the spectrum of TC4 suggests that the object is optically bright E-type rather than a low albedo P-type.

8. Characterization: Radar observations

The extremely close approach by 2012 TC4 was expected to yield radar signal-to-noise ratios of roughly 10^6 per day at Goldstone and Arecibo and provide an outstanding opportunity to investigate the physical properties of this object. We scheduled observations on several telescopes between 2017 October 9–14, dates that straddled the closest approach on October 12. The most extensive radar observations occurred using monostatic and bistatic configurations with the 70 m DSS-14 (8560 MHz, 3.5 cm) and 34 m DSS-13 (7190 MHz, 4.2 cm) antennas at the Goldstone Deep Space Communications Complex and the 100 m Green Bank Telescope (Table 7). In addition, on October 11, we transmitted with DSS-14 and received radar speckle observations with elements of the Very Long Baseline Array. 2012 TC4 was also observed with radar in Australia using NASA's 34 m DSS-36 antenna (7190 MHz) at Tidbinbilla to transmit and the six-element Australian Telescope Compact Array to receive (Abu-Shaban et al., 2018). Radar observations had been planned at Arecibo but did not occur due to damage caused by Hurricane Maria, which suspended radar observations at Arecibo for nearly three months. The radar observations described below utilized data acquisition and reduction techniques that have been discussed extensively in the literature (Ostro et al., 2002 and earlier references therein) so we do not repeat them here. Here we summarize first results from radar observations at Goldstone and Green Bank; results from Australia will be reported separately elsewhere.

8.1. Overview of the radar observations

Due to the asteroid's changing distance from day to day during the radar observations, and up to a factor of two within one of the tracks on October 12, our observing strategy changed daily to utilize the highest resolutions obtainable given the SNRs. Prior to the beginning of the radar observations, observations obtained at Palomar suggested that 2012 TC4 might be an optically-dark object, and given the absolute magnitude of 26.7, we were expecting a diameter of roughly 40 m. The echo bandwidth (or Doppler broadening) is given by $B = 4piD\ \cos d/(\lambda P)$, where D is the diameter, P is the rotation period, d is the subradar latitude, and λ is the radar wavelength. For a rotation period of ~12 min and a diameter of ~40 m, we expected to measure a bandwidth of about 20 Hz.

Echo power spectra obtained on October 9 and 10 (Fig. 13) yielded bandwidths of < 10 Hz and signal-to-noise ratios that were much

Table 7
Observational circumstances for radar data.

Setup					Start–End			Dist.
	Range	Freq	Soln	Runs	HHMMSS	TX	RX	A.U.
2017 Oct. 9								
CW		1.0	50	416	071257–094440	DSS14	DSS14	0.011
2017 Oct. 10								
CW		2.0	57	71	055838–061709	DSS14	DSS14	0.008
Ranging	1500	3.1	57	105	062347–065129	DSS14	DSS14	
Ranging	1650	2.8	57	179	065641–074404	DSS14	DSS14	
Ranging	150	1.9	63	122	075343–082555	DSS14	DSS14	
Ranging	18.75	1.5	65	94	083540–090020	DSS14	DSS14	
2017 Oct. 11								
Ranging	15	2.0	67	20	060606–060920	DSS14	DSS14	0.0038
Imaging	3.75	1.0	67	122	071525–073455	DSS14	DSS14	
CW		1.0	67		0816–0840	DSS14	DSS13	
CW		1.0	67		0845–0915	DSS14	VLBA	0.0033
2017 Oct. 12A								
CW		1.0	71		0220–0248	DSS13	GBT	0.00066
Imaging	1.875	0.4	71		0313–0322	DSS13	GBT	0.00052
Transmitter power = 40 kW								
2017 Oct. 12B								
CW		1.0	71		1245–1305	DSS13	GBT	0.0012
Imaging	1.875	0.4	71		1310–1930	DSS13	GBT	
CW		1.0	71		1904–1930	DSS13	GBT	0.0023
Transmitter power = 40 kW until 13:40 and 70 kW afterward								
2017 Oct. 14								
CW		1.0	71	66	114,011–115,947	DSS14	DSS14	0.009
Ranging	75	1.5	71	95	121,952–124,804	DSS14	DSS14	
Ranging	18.75	2.4	5 71	111	125,215–132,501	DSS14	DSS14	

Setup: type of observation conducted.
CW: continuous wave acquisition of echo power spectra.
Ranging and Imaging: delay-Doppler observations.
Range:range resolution in meters.
Freq: Doppler frequency resolution in Hz.
Soln: orbital solution number used to compute the ephemerides. We updated the orbit numerous times using radar and optical astrometry.
Runs: number of transmit-receive cycles used with each setup for monostatic observations. This column is left blank for bistatic observations.
Start and End: UTC receive start and stop times in abbreviated hh:mm:ss format.
TX: antenna used to transmit.
RX: antenna or array used to receive.
*Transmitter powers at DSS-14 were ~440 kW. Transmitter powers at DSS-13 varied with elevation due to airspace restrictions.
**On October 11 and 12 we give the distance at the start and end of the track.

weaker than expected. This was the first hint that this object might be much smaller than 40 m in diameter. On October 9, the SNRs were weak and we obtained only continuous wave (CW) echo power spectra; but on October 10, the SNRs were several times stronger and we obtained ranging observations that we used to update the orbit and echo power spectra to estimate radar cross sections, circular polarization ratios, and echo bandwidths. The highest range resolution obtained on October 10 was 18.75 m/pixel, which did not resolve the echo in range due to the asteroid's small size.

On October 11, the distance had shrunk to < 0.004 AU (1.6 lunar distances) and the SNRs were much stronger, so we obtained a mixture of monostatic observations using DSS-14 to transmit and receive and bistatic observations that used DSS-14 to transmit and DSS-13 to receive. The round-trip light travel time was so short that monostatic observations were very challenging due to the time it takes to switch from transmit to receive configurations. During the monostatic observations, each transmit/receive cycle integrated only about 0.7 s of data and about 3 s of noise, but the SNRs were so strong that receiver noise was negligible. The echo power spectra in observations spanning about 24 min showed pronounced bandwidth variations that are indicative of an elongated shape. We obtained about 20 min of monostatic delay-Doppler images with a resolution of 3.75 m/pixel, which is the finest range resolution available at DSS-14 (Slade et al. 2011). This resolution placed only 1–2 range pixels on the asteroid, covered considerable rotation, and established that 2012 TC4 has a long axis of < 20 m.

Two tracks were scheduled on October 12 about 3 h before and 7 h after the closest approach when the SNRs at Goldstone were strongest. 2012 TC4 was too far south at the moment of closest approach for Goldstone to track; but it was observed successfully at that time with radar in Australia (Abu-Shaban et al., 2018). The round-trip light travel times during the October 12 Goldstone tracks were too short for monostatic observations at DSS-14, and the SNRs were extremely strong, so we transmitted continuously with DSS-13 and received at the Green Bank Telescope, a bistatic configuration that is ideal for imaging very close NEAs. DSS-13 is much less sensitive as a transmitter than DSS-14 due to its smaller aperture (34 m vs. 70 m), lower transmitter power (80 kW vs. 440 kW), and lower gain, but it is the transmitter of choice for imaging extremely close targets where the signal-to-noise ratio is not a limiting factor (Naidu et al., 2016) because DSS-13 can achieve a range resolution of 1.875 m/pixel, which is two and four times finer than the highest range resolutions available at DSS-14 and Arecibo (Benner et al., 2015).

The SNRs during both tracks on October 12 were extremely strong and we obtained images with a range resolution of 1.875 m/pixel. This was the first time that resolution was used on a solar system target and these were also the highest resolution radar images of an asteroid ever obtained with Goldstone (Table 7). By October 14, the asteroid's

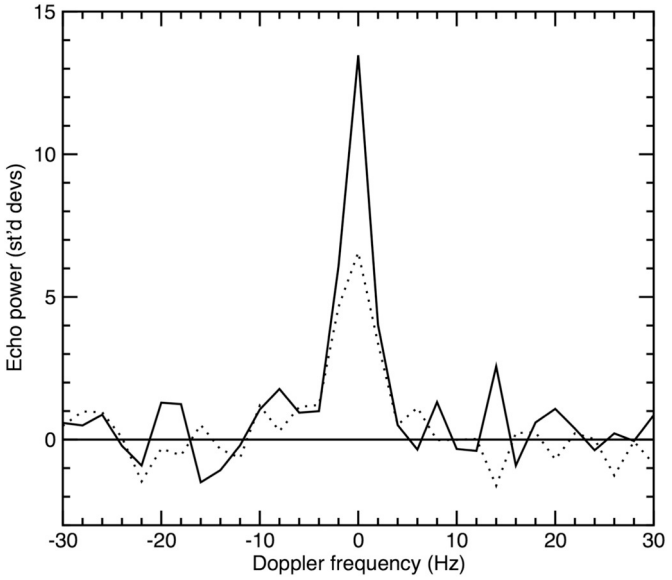

Fig. 13. Echo power spectrum obtained at DSS-14 on October 10. Echo power in standard deviations of the noise is plotted as a function of Doppler frequency. The frequency resolution is 2 Hz. The spectrum is a weighted sum of 71 transmit-receive cycles. Solid and dashed curves show echo power in the opposite-sense circular (OC) and same-sense circular (SC) polarizations.

distance increased to 0.009 AU and the SNRs were a factor of ~300 lower than at the peak, so we concluded the radar campaign with echo power spectra and monostatic ranging measurements to update the orbit. During the tracks on October 9, 10, 11, 12, and 14, we obtained two Doppler and seven time-delay measurements and used them to update the orbital solutions in real time using our On-Site Orbit Determination (OSOD) software (Table 7). Orbital solution (#71) had sufficiently small uncertainties that we used it on the final three tracks. The radar astrometry significantly reduced the orbital uncertainties and helped eliminate all possible impact solutions in the next century (discussed earlier in this paper).

8.2. Physical properties

Fig. 13 shows a representative echo power spectrum obtained at DSS-14 on October 10. The figure shows a weighted sum of data spanning 18.5 min that covers more than one full ~12 min period. The spectrum shows a narrow bandwidth. The ratio of echo power in the same sense (SC) to opposite sense (OC) of circular polarization is about 0.55. The frequency resolution of 2 Hz barely resolves the echo.

Echo power spectra obtained on dates when the asteroid was closer are much stronger and show considerably more detail. Fig. 14 shows a series of echo power spectra displayed as one-dimensional images that have been stacked vertically. Shown in this manner, where time increases downward, the spectra show rapid and pronounced bandwidth variations as a function of time with a fundamental period of roughly 11–12 min that is consistent with the 12-minute principal period evident in the lightcurves. However, the pattern does not appear to repeat in a regular fashion, as it should for a principal axis rotator, and to zeroth order, the progression evident in Fig. 13 is also consistent with a non-principal axis spin state. The Doppler broadening of the echoes varies dramatically by about a factor of two as a function of time and confirms that the asteroid is highly elongated. The oscillations of the echoes between negative and positive Doppler frequencies are also evidence for an asymmetric shape.

We obtained more than 6 h of bistatic DSS-13/Green Bank 1.875 m resolution delay-Doppler imaging on October 12. Fig. 15 shows a representative sample spanning 47 min obtained about 6 h after the closest approach. Although the capability to image objects at 1.875 m resolution has existed since 2015, this was the first time that this capability had been tested on an asteroid. Even at such a high range resolution, 2012 TC4 is so small that the images resolve the asteroid into only a few rows in time delay, and detailed features are not visible.

Due to the rapid rotation, we grouped the images covering intervals of only 20 s per frame as a compromise between achieving adequate signal-to-noise ratios vs. excessive rotational smear. The frequency resolution is 0.4 Hz, so each image is a weighted sum of only 8 Fast-Fourier Transforms (FFTs) or "looks." Consequently, there is considerable self-noise at frequencies containing echo power which needs to be taken into account when interpreting apparent brightness fluctuations in the images.

The images show an object whose bandwidth in Doppler frequency and extent in time delay vary by about a factor of two as it spins. The number of range pixels with echo power above the noise threshold places a lower bound on the long axis of at least 12 m. The true extent of the long axis is almost certainly larger and would be double the visible extent if this object were a sphere. 2012 TC4 is clearly not a sphere, so

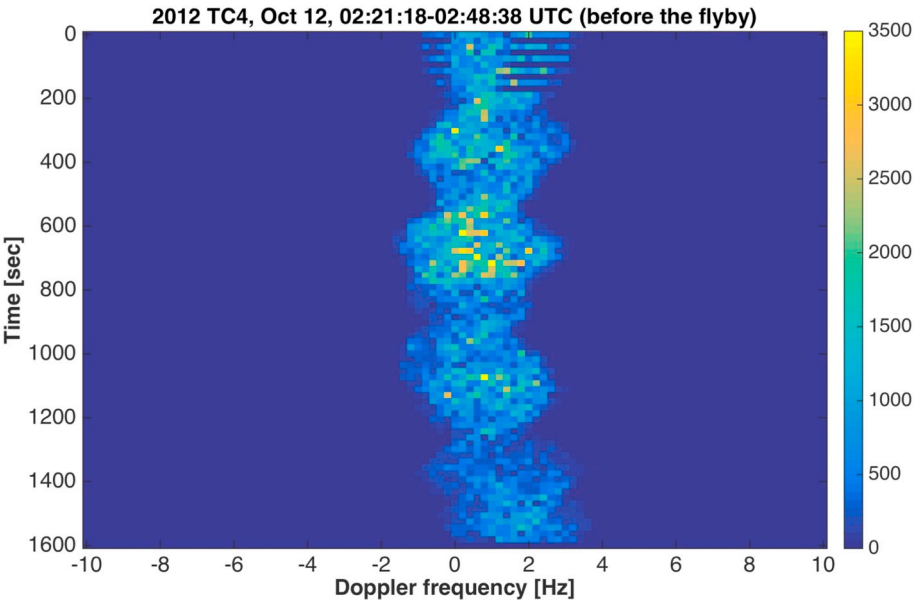

Fig. 14. Sequence of echo power spectra obtained between 02:21:18–02:48:38 UT on October 12 that have been converted to one-dimensional images and then stacked vertically. Time increases from top to bottom and Doppler frequency increases from left to right. The signal-to-noise ratios are given in the scale bar on the right. The frequency resolution is 0.2 Hz. Echo power spectra displayed in this manner show pronounced bandwidth variations as the asteroid spins. The offset from zero Hz indicates that Doppler corrections were not applied to the ephemeris prior to obtaining the data. The displacement of the echoes relative to zero Hz is due to variations in the Doppler uncertainties with time and in the accuracy of the Chebyshev polynomials used to compute the ephemerides.

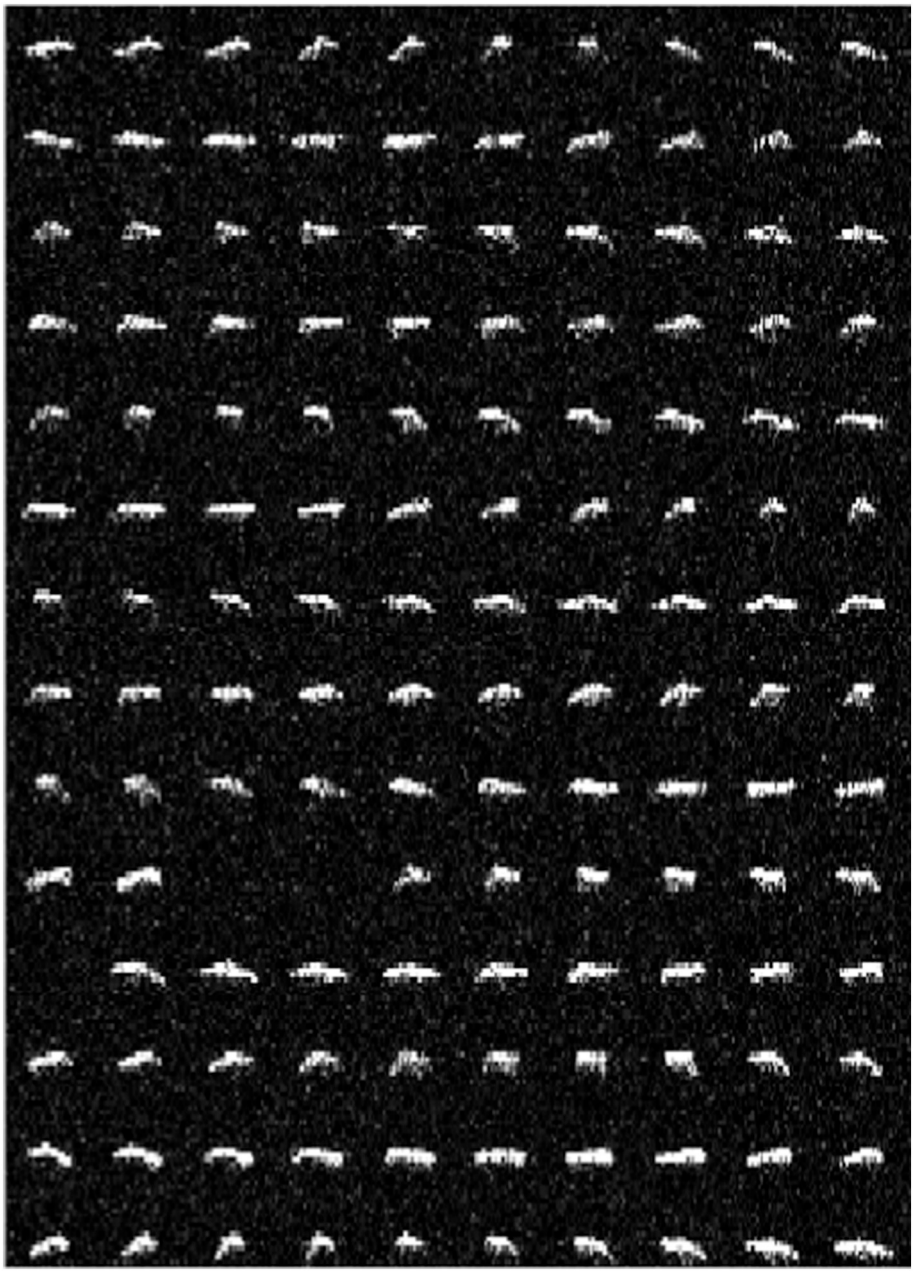

Fig. 15. Sequence of delay-Doppler images obtained on October 12 between 13:09:44–13:56:24 UTC. DSS-13 was used to transmit and the Green Bank Telescope was used to receive. In each frame, time delay (range) increases from top to bottom and Doppler frequency increases from left to right, so rotation is counterclockwise. Resolution is (1.875 m) × 0.4 Hz. Time increases to the right and down. Each frame is a weighted sum of 20 s of data. Drift of the echo in time delay is evident. Blank panels in rows 10 and 11 indicate gaps in the data taking. (For interpretation of the references to color in this figure legend, the reader is referred to the web version of this article.)

we do not believe that the long axis is substantially > 12 m. If the line-of-sight were close to the equator, then the visible extent would shrink even more than it does in the images, thus the images suggest that the instantaneous sub-radar latitudes were not equatorial and that the true extents are not double the visible extents. Based on the visible extents in the radar images, we estimate an effective diameter of roughly 10 m. Obtaining a more precise diameter estimate requires 3D modeling that is beyond the scope of this paper. Given its absolute magnitude of 26.7, a diameter of ~10 m corresponds to an optical albedo in the realm of 0.4, which implies that 2012 TC4 is optically bright.

The images reveal an angular, asymmetric object with multiple facets that is reminiscent of NEAs 2003 MS2 (Lawrence et al., 2015) or 2010 AL30 (Slade et al., 2010). 2012 TC4 is among the smallest asteroids imaged by radar to date (Brozovic et al., 2016). When shown as an animation, the images display rotation about the long axis that is consistent with the non-principal axis rotation inferred from the lightcurves. Given the rapid rotation, it seems clear that 2012 TC4 has cohesive strength, although the forces required to keep it together could be quite feeble (Scheeres et al., 2015).

In principle, the delay-Doppler images and echo power spectra could be inverted to estimate the 3D shape, but due to the non-principal axis spin state, the parameter space of possible solutions is enormous and shape estimation using only radar data would be a lengthy process and might not provide a unique solution. Fortunately, an extensive set of lightcurves is also available and can be used to independently estimate the spin state. We will report the results of 3D shape estimation in the future after a detailed spin state is available from the photometry (P. Pravec, pers. comm.), which will accelerate 3D shape estimation dramatically. Once a 3D model is available, estimation of the area/mass ratio due to solar radiation pressure (discussed earlier) should permit computation of the mass and bulk density, which will provide the first such estimates for an asteroid in this size regime and important insight into the interior structure.

8.3. Disk-integrated radar properties

The ratio of echo power in the same sense (SC) to opposite sense (OC) of circular polarization, SC/OC, is a zeroth-order gauge of near-surface roughness. For 2012 TC4, we observed day-to-day variations between 0.50 and 0.65 with an average of 0.57 ± 0.08. The scatter in the measurements is relatively common among NEAs with widely varying SNRs. The average SC/OC, 0.57, is relatively high among near-Earth asteroids observed by radar to date; for comparison, Benner et al. (2008) found a mean of SC/OC = 0.34 ± 0.28 from a sample of 214 NEAs observed at Arecibo and Goldstone. Subsequent observations of hundreds of additional NEAs have yielded similar results (Taylor et al., 2012; Benner et al., 2015).

The high circular polarization ratio is consistent with the upper end of the distribution observed for SQ- and C-class NEAs (Benner et al., 2008) and with the lower end of the V-class NEA distribution but it is statistically significantly lower than the distribution observed for *E*-class NEAs. If only the radar data were considered, we might conclude that 2012 TC4 is mostly likely a C- or SQ-class object based on its circular polarization ratio. However, given the results from photometric colors and spectroscopy, and the conclusion discussed below from delay-Doppler images that 2012 TC4 is optically-bright, then it's clear that TC4 isn't a P- or an M-type, so E seems most likely. If so, then its circular polarization ratio is the lowest observed among near-Earth objects for that spectral class, which have a mean of 0.89+-0.08 (Benner et al.) and a minimum of 0.74 (for 4660 Nereus; Benner et al., 2008). To date, only two metallic NEAs have been identified and both have SC/OC < 0.2 which is dramatically less than that of 2012 TC4. It seems unlikely that this asteroid is metallic. The circular polarization ratio is comparable to that of 2006 RH120, an even smaller NEA with a diameter of ~3 m observed at Goldstone in 2007 (Brozovic et al., 2016). Among 34 NEAs observed by radar with absolute magnitudes fainter than 22 reported by Benner et al. (2008), the circular polarization ratio of 2012 TC4 ranks fifth highest, establishing that the surface of this object is unusual. High circular polarization ratios can be caused by a variety of mechanisms such as near-surface roughness, curvature at scales comparable to that of the radar wavelength, and a high refractive index (Virkki et al., 2014; 2015). The relatively high circular polarization ratio is also consistent with the preliminary conclusion above that 2012 TC4 is optically bright.

Weighted sums of echo power spectra yield an average radar cross section of 7.4×10^{-6} km^2 ± 35%, where we have adopted a conservative uncertainty to incorporate systematic pointing and calibration errors. When a precise effective diameter becomes available from 3D modeling, we will use it to obtain the radar albedo, which will provide an important constraint on the near-surface density, composition, and possibly the spectral class.

8.4. Discussion

How did 2012 TC4 acquire its angular, elongated shape? It seems plausible that this object could be a fragment ejected from a larger object during a collision. Laboratory impact experiments have produced elongated and angular shapes consistent with the shape inferred from the radar images (Holsapple et al., 2002, and earlier references therein). The rapid, non-principal axis spin state could originate in a similar manner, but the current spin state is probably also affected by the YORP effect (Vokrouhlicky et al., 2015) and perhaps tides from close terrestrial encounters, so it is unlikely to be primordial.

Did the spin state of 2012 TC4 change during the 2017 flyby due to terrestrial tides? This possibility has been investigated theoretically for other very closely approaching NEAs such as Apophis in 2029 (Scheeres et al., 2005) and has been directly observed with (4179) Toutatis using 3D shape and spin state modeling from Goldstone and Arecibo radar images obtained at five apparitions between 1992 and 2008 (Takahashi et al., 2013). Detecting spin changes requires detailed observations before and after closest approach, so in principle this might be possible using a combination of lightcurves obtained before the flyby and high-resolution radar images obtained only hours before and after the flyby. The non-principal axis spin state complicates this effort considerably, so this will be the topic of future work after an estimate of the spin state is available from the photometry.

9. Impact risk assessment

Recently, probabilistic impact risk assessment methods, which combine sampling of uncertain asteroid properties with efficient physics-based entry and damage models, have been used to evaluate the risk due to impacts from the overall population of near-Earth asteroids (e.g., Mathias et al., 2017; Stokes et al., 2017; Rumpf et al., 2017). Such models can also provide rapid assessment of potential ground-damage risks to support mitigation and response decisions in the event that a specific impact threat is discovered. In order to evaluate how those methods would apply to a specific case, and how the resulting risk assessments would unfold as additional information is obtained about a real object, probabilistic impact risk assessments were performed for hypothetical impactors based on the 2012 TC4 close approach in October 2017. In parallel with the observation campaign of the real 2012 TC4, we considered a synthetic trajectory similar to that of 2012 TC4 but leading to an impact during the October 2017 encounter. As new astrometric observations of 2012 TC4 were collected, we generated simulated observations for the synthetic impactor, updated the orbital assessment, and computed a hypothetical impact swath of 1000 potential atmospheric entry points based on Monte Carlo orbital samples. Each entry point along the swath was defined with the initial coordinates, velocity, angle, and azimuth of the initial atmospheric entry at 100 km altitude.

The impact risk along the evolving swath was assessed using the Probabilistic Asteroid Impact Risk (PAIR) model of Mathias et al. (2017), with the asteroid property distributions, damage models, and affected population metrics employed in Stokes et al. (2017). For each of the 1000 hypothetical entry points, 1000 probabilistic impact cases were simulated by sampling uncertainty distributions for the asteroid's unknown pre-entry characteristics (albedo, density, and aerodynamic strength parameters). Atmospheric entry and breakup were modeled for each hypothetical impact case using the Fragment-Cloud Model approach (Wheeler et al., 2017) to calculate the energy deposited in the atmosphere, the airburst altitude, any remaining energy striking the ground, and the coordinates of the impact or airburst point along the entry trajectory. The extent of the damage resulting from blast waves, thermal radiation, and tsunami was computed, and the number of people affected was calculated from the local population within the damage regions.

The risk assessment was performed at several epochs before and during the close approach of 2012 TC4, each time incorporating new information about 2012 TC4 as it became available. For instance, the spread in the hypothetical entry locations was reduced as improved astrometry became available. The synthetic trajectory used for this assessment produced very low entry velocities of around 11.85 km/s, and shallow entry angles of under 20° from the horizontal. For the initial epochs, the full asteroid property distributions employed by Stokes et al. (2017) were used, including sizes based on the full albedo distribution (Mainzer et al., 2011) and property distributions representing three compositional types: anhydrous stones with albedos ≥0.1, hydrous stones with albedos < 0.1, and irons with any albedo. For later epochs, additional observational data enabled the property distributions to be further constrained by compositional type and improved radar sizing estimates.

At each epoch, impact scenarios were run for two different size cases: one for an H = 26.7 object and one for an H = 21.9 object. The smaller size was chosen to match 2012 TC4's known parameters, while the larger size was chosen to provide a higher-damage scenario similar

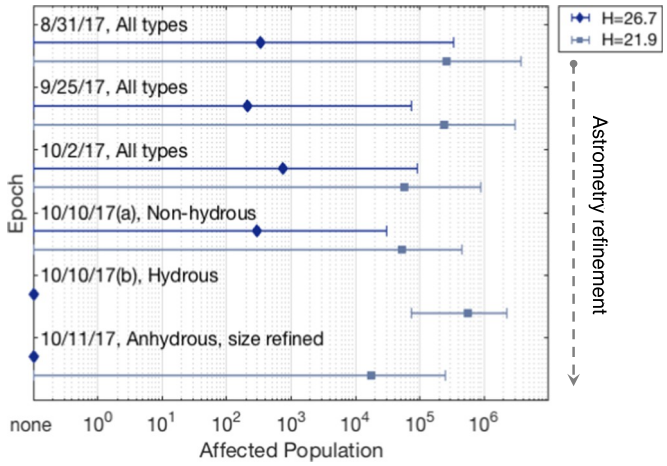

Fig. 16. The affected population results from impact risk assessments of 6 epochs for a hypothetical TC4-based H = 26.7 object and a larger hypothetical H = 21.9 object. The diamonds/squares show the mean affected population and the bars show the minimum and maximum values across all simulations run for each epoch. Except for the hydrous-only epoch of the larger H 21.9 case, all other sets included instances where the affected population was zero.

to the hypothetical impact exercise performed for the 2017 Planetary Defense Conference. For simplicity, the same synthetic impact swath points were used for both size cases in this assessment. However, we note that actual impact location estimates may be more readily constrained for a larger object than for a smaller one. A summary of the hypothetical affected population results for the two size cases across all epochs is shown in Fig. 16, and a comparison of the associated swath damage areas is shown in Fig. 17. Details about each epoch and the input ranges considered are given in the next subsection below. A more detailed description of the range of possible outcomes and their dependence on geography are beyond the scope of this paper.

10. Risk assessment: Timeline of epochs

10.1. 2017 August 31

The simulated atmospheric entry points (at 100 km altitude) for this initial epoch are shown in Fig. 18. The entry velocity was ~11.85 km/s traveling generally east-southeast, and the entry angle ranged from 20° down to 12° over the length of the swath. The hypothetical impact/airburst points resulting from the entry simulations were spread along a track ~1650 km long across North Carolina. The size distribution was determined by combining absolute magnitude with an albedo distribution based on the measurements tabulated by Mainzer et al. (2011). The Stokes et al. (2017) distribution of 60% anhydrous stones (albedo ≥ 0.1), 35% hydrous stones (albedo < 0.1), and 5% irons (any albedo) was used. Similarly, the density and strength distributions for these types were identical to those used in Stokes et al. (2017).

10.2. 2017 September 25

Improved astrometry resulted in a shortening of the track of hypothetical impact points to ~470 km. The entry angles over the refined swath were 18–16°. All other inputs were identical to the 8/31/17 epoch.

10.3. 2017 October 02

The g, r, and i colors discussed in the *Colors and Spectroscopy* section were compared to the location of different taxonomic classes in griz space in DeMeo and Carry (2013) and hydrous stones were ruled out as a possibility. The incoming objects in the Monte Caro runs for this epoch were presumed to be 92.3% anhydrous stones and 7.7% irons. The size distribution was still derived from H and the albedo distribution, but the albedo distribution was modified to remove values likely to be associated with hydrous stones. Improved astrometry resulted in a shortening of the track of hypothetical impact points to ~220 km for the H = 26.7 object and ~190 km for the larger object, with entry angles now constrained closely around 17°.

10.4. 2017 October 10

Improved astrometry resulted in a further shortening of the track of hypothetical impact points. An initial, weak radar detection implied an effective diameter of ~10 m. When coupled with H = 26.7, this implies an albedo of ~0.37. Hydrous stones generally have albedos < 0.1, so this radar measurement was consistent with the non-hydrous composition conclusion from the g,r,i colors. However, an optical spectrum was also concurrently measured (as discussed in *Colors and Spectroscopy* section) that was most consistent with a C-type, equivalent to the hydrous stone category from Stokes et al. (2017). Given the uncertain and conflicting information about composition available at this time, two risk assessment runs were performed. The epoch labeled 10/10/17a excluded hydrous stones. Other than the hypothetical impact points, the input distributions were identical to the 10/2/17 epoch. The hypothetical impact track was ~120 km for the smaller object and ~85 km for the larger object. In contrast, the epoch labeled 10/10/17b assumed the incoming object was definitely a hydrous stone. The size distribution was generated from the H magnitude and the portion of the Mainzer et al. (2011) albedo distribution < 0.1. The densities and strengths were calculated according to the paradigm set out for hydrous stones in Stokes et al. (2017). For this composition, there were no ground impacts or airbursts low enough to cause damage for the smaller object. The hypothetical impact track for the larger object was ~45 km long.

10.5. 2017 October 11

An infrared spectrum (described in the *Colors and Spectroscopy* section) was combined with the previously reported optical spectrum to lead to the conclusion that TC4 is within the anhydrous stones category from Stokes et al. (2017). For all the parameters related to composition (e.g., density, strength), the Monte Carlo engine sampled from the anhydrous stone distributions. The size distribution was refined based on the reported radar measurements. The analysis of the radar measurements available at this time indicated that the long axis was > 12 m and much shorter than 24 m. The aspect ratio between the longest and shortest axes was reported to be ~2. We developed a model of a range of ellipsoids consistent with the radar observations and then calculated their effective spherical diameters. For the H = 26.7 object, this model yielded an effective diameter distribution described by a truncated Gaussian with a mean of 10.6 m, a width of 2.5 m, and a lower limit of 6.6 m. This model was translated into the corresponding albedos for the H = 26.7 object. These albedos were then also used to describe the size distribution for the H = 21.9 case. None of the smaller virtual impactors resulted in ground damage. Improved astrometry resulted in a shortening of the track of the hypothetical impact points of the H = 21.9 object to ~42 km.

11. Risk assessment: Discussion

For both sizes considered in this particular scenario, the improvements in astrometry led to moderate reductions in the uncertainty in the range of possible outcomes. However, in all epochs, impact with the Earth was assured and the hypothetical impact corridor always included moderately populated areas, so dependence on astrometry should be expected to be minimal. When considering a less controlled scenario, astrometry becomes critical in determining whether an impact

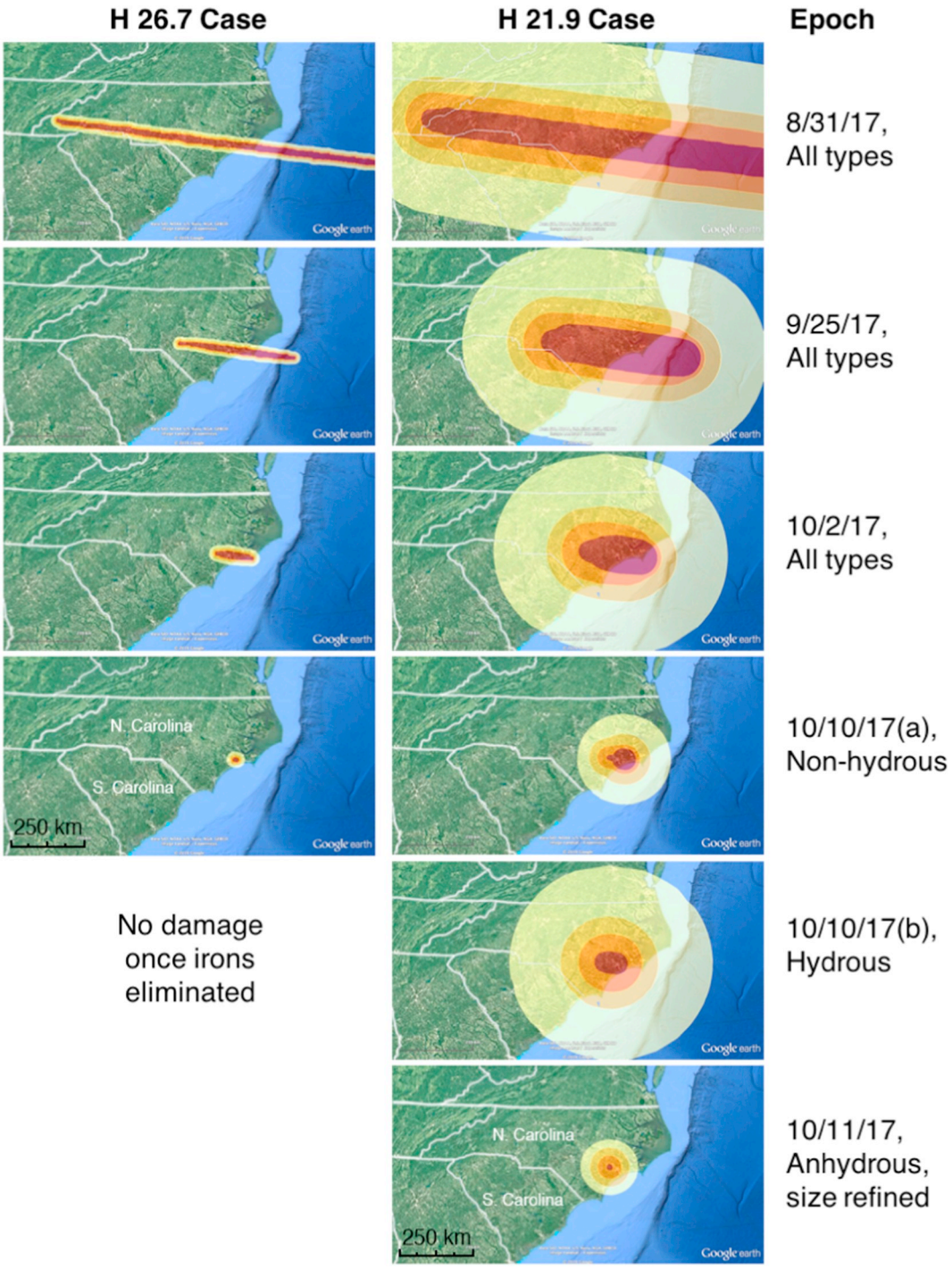

Fig. 17. Damage maps showing the extent of the potential damage zones along the swath for each epoch, with blast overpressure levels of ≥1 psi (yellow), ≥2 psi, ≥4 psi, and ≥10 psi (red). All maps are shown on the same scale for a comparative overview of the relative damage sizes, with the full frame covering an area roughly 1200-by-630 km centered over North Carolina, U.S. Maps were generated in Google Earth (Map data: Image Landsat/Copernicus; Data SIO, NOAA, U.S. Navy, NGA, GEBCO). (For interpretation of the references to color in this figure legend, the reader is referred to the web version of this article.)

occurs at all and whether it is coincident with a populated area. Across the epochs, only the irons caused significant damage for the smaller (H = 26.7) size. If a strong, non-fracturing iron was not a possibility, then no damage was predicted. Given the slow, shallow entry conditions of this particular scenario, the weaker stone types burst at too high of an altitude with too little energy to cause notable ground damage. For the larger (H = 21.9) size, hydrous stones caused the greatest damage, anhydrous stones caused the least damage, and irons caused moderate damage. The hydrous stones cause the most damage due to their lower albedo range (< 0.1) yielding the largest sizes. Despite being stronger and denser, the iron types cause less damage because they over-penetrated below the optimal burst altitude for their larger impact energies. For a given burst energy, there is an optimal height-of-burst altitude that will yield the greatest possible blast damage on the ground (Aftosmis et al., 2017). For small objects, the optimal burst altitude is quite low and the ground-impacting cases that cause more damage than the high-bursting cases. For larger objects, however, the optimal burst altitude is quite high, and weaker compositions that begin

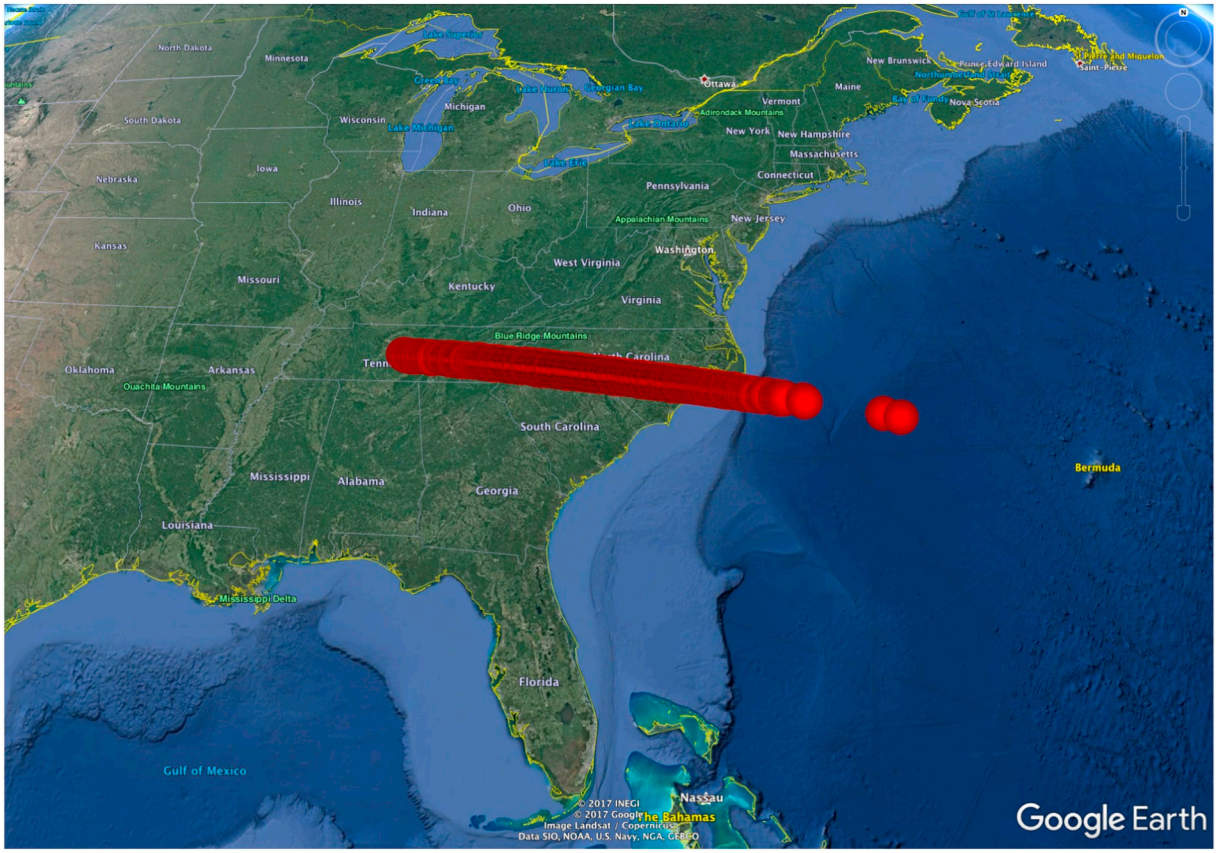

Fig. 18. Map of the simulated atmospheric entry points at 100 km altitude, based on the available astrometric observations on 8/31/2017. (Map data: INEGI, Google; Image Landsat/Copernicus; Data SIO, NOAA, U.S. Navy, NGA, GEBCO).

to disrupt higher up can yield greater damage. The different dependence on composition observed for the different sizes considered highlights that, after astrometry, size is the most important physical property to determine for an incoming object.

12. Summary

We conducted a community-led global planetary defense exercise with guidance from NASA Planetary Defense Coordination Office. The target of our exercise was 2012 TC4, an ~10 m diameter asteroid that made a close pass by the Earth on 2017 October 12 at a distance of about 50,000 km. The goal of TC4 observing campaign was to recover, track, and characterize 2012 TC4 as the hypothetical impactor in order to exercise the global planetary defense system including observations, modeling, predictions, and communication. We summarize key findings from this campaign below:

- The orbit of 2012 TC4 significantly changed after its 2012 close approach with the Earth such that the semi-major axis increased from 1.3 to 1.4 AU and the orbital period went from 1.45 to 1.67 yr. Due to this, 2012 TC4 moved into a 5:3 resonance with the Earth, leading to a second encounter on 2017 October 12. Early in 2017, the circumstances of the encounter were still largely uncertain based on the 2012 orbit with a 3-sigma range for the geocentric close approach distance was 13,000 km to 290,000 km.

- The first opportunity to recover 2012 TC4 occurred during the summer of 2017, a couple months before the 2017 October 12 encounter. During this time frame, 2012 TC4 became progressively brighter but the plane-of-sky uncertainty grew larger. To minimize the area of the sky to be searched, we made a recovery attempt with ESO's Very Large Telescope (VLT) on Cerro Paranal (Chile), which is capable of detections as faint as V ~ 27. To support the recovery attempts and refine the ephemeris estimate, we reanalyzed the 2012 observational data. We made three attempts on 2017 July 27, 31 and August 5 and recovered 2012 TC4 within its expected uncertainty 2.2 arcmin from the nominal prediction. The first automatic detection by the Pan-STARRS1 pipeline was on September 25, which is the earliest that 2012 TC4 would have been discovered in survey mode if it had not been known prior to 2017.

- We characterized 2012 TC4 using photometry, spectroscopy, and radar techniques. Based on photometric observations, we determined a rotation period of 12.2 min with an amplitude of 0.9 magnitudes. An additional lower amplitude period was detected indicating that 2012 TC4 was in a state of non-principal axis rotation. Broadband color observations led to B-V: 0.64 ± 0.06, V-R: 0.44 ± 0.04, and V-I: 0.85 ± 0.06 which are consistent with its flat and featureless visible and near-IR spectra of an optically bright object. The various datasets accumulated in the course of this campaign did not find consensus on a taxonomic classification, but it is not unreasonable to place 2012 TC4 in the Tholen X-class (Tholen, 1984).

- Radar images at 1.875 m resolution placed only a few range pixels on the asteroid, reveal an angular, asymmetric, and elongated shape, and establish that 2012 TC4 is less than 20 m on its long axis. We estimate a circular polarization ratio of 0.57 + -0.08 that is relatively high among NEAs observed to date by radar. High circular polarization ratios can be caused by a variety of mechanisms such as near-surface roughness, curvature at scales comparable to the radar wavelength, and a high refractive index.

- We performed probabilistic impact risk assessments for hypothetical impactors based on 2012 TC4 parallel with the observation campaign of the real 2012 TC4. The risk assessment was calculated at several epochs before and during the close approach of 2012 TC4, each time incorporating new information about 2012 TC4 as it became available. Across the epochs, we found that only the irons caused significant damage for the smaller (H = 26.7) size. If a strong, non-fracturing iron was not a possibility, then no damage was predicted. For the larger (H = 21.9) size, hydrous stones caused the greatest damage (due to their lower albedos yielding larger sizes), anhydrous stones caused the least damage, and irons caused moderate damage. The different dependence on composition observed for the different sizes considered highlights that, after astrometry, size is the most important physical property to determine for an incoming object.

Acknowledgments

The Green Bank Observatory is a facility of the National Science Foundation operated under cooperative agreement by Associated Universities, Inc. This research has made use of the KMTNet system operated by the Korea Astronomy and Space Science Institute (KASI) and the data were obtained by observations made at the South African Astronomical Observatory (SAAO). This work is partially supported by the South African National Research Foundation (NRF). This work is supported in part by the National Aeronautics and Space Administration (NASA) under grant No. NNX15AE90G issued through the SSO Near-Earth Object Observations Program and in part by a grant from NASA's Office of the Chief Technologist.

References

Abu-Shaban, Z., Benson, C., Boyce, R., Benner, L.A.M., Lazio, J., Slade, M.A., Stacy, N., Baines, G., Horiuchi, S., Kruzins, E., Edwards, P., Phillips, C., Reynolds, J., Stevens, J., 2018. Planetary radar. In: Asteroids Observation From the Southern Hemisphere Using Planetary Radar, Presented at The Committee on Space Research (COSPAR) 2018, Pasadena, CA, USA, 14–22 July 2018.

Aftosmis, M.J., Mathias, D.L., Tarano, A.M., 2017. Simulation-based height of burst map for asteroid airburst damage prediction. Acta Astronaut. https://doi.org/10.1016/j.actaastro.2017.12.021. (ISSN 0094-5765).

Alvarez, L.W., Alvarez, W., Asaro, F., Michel, H.V., 1980. Extraterrestrial cause for the cretaceous-tertiary extinction. Science 208, 1095–1108. https://doi.org/10.1126/science.208.4448.1095. (June).

Benner, L.A.M., Ostro, S.J., Magri, C., Nolan, M.C., Howell, E.S., Giorgini, J.D., Jurgens, R.F., Margot, J.-L., Taylor, P.A., Busch, M.W., Shepard, M.K., 2008. Near-Earth. Asteroid surface roughness depends on compositional class. Icarus 198, 294–304. https://doi.org/10.1016/j.icarus.2008.06.010.

Benner, L.A.M., Busch, M.W., Giorgini, J.D., Taylor, P.A., Margot, J.-L., 2015. Radar Observations of Near-Earth and Main-Belt Asteroids. pp. 165–182. https://doi.org/10.2458/azuuapress9780816532131-ch009.

Binzel, R.P., DeMeo, F.E., Bus, S.J., Tokunaga, A., Burbine, T.H., Lantz, C., Polishook, D., Carry, B., Morbidelli, A., Birlan, M., Vernazza, P., Burt, B.J., Moskovitz, N., Slivan, S.M., Thomas, C.A., Rivkin, A.S., Hicks, M.D., Dunn, T., Reddy, V., Sanchez, J.A., Granvik, M., Kohout, T., 2019. Compositional Distributions and Evolutionary Processes for the Near-Earth Object Population: Results from the MIT-Hawaii Near-Earth Object Spectroscopic Survey (MITHNEOS). https://doi.org/10.1016/j.icarus.2018.12.035.

M. Brozovic, L. A. M. Benner, M. W. Busch, J. D. Giorgini, M. A. Slade, and K. J. Lawrence. Recent Goldstone radar observations of selected near-Earth asteroids less than 140 m in diameter. In S. R. Chesley, A. Morbidelli, R. Jedicke, and D. Farnocchia, editors, Asteroids: New Observations, New Models, volume 318 of IAU Symposium, pp. 160–169, 2016. doi:https://doi.org/10.1017/S1743921315008807.

Carbognani, A., 2014. Asteroids lightcurves at OAVdA: 2013 December–2014 June. In: Minor Planet Bulletin. 41. pp. 265–270.

Chodas, P.W., 1999. Orbit uncertainties, keyholes, and collision probabilities. In: Bulletin of the American Astronomical Society. vol. 31. Bulletin of the Astronomical Society, pp. 1117.

DeMeo, F.E., Carry, B., 2013. The taxonomic distribution of asteroids from multi-filter all-sky photometric surveys. Icarus 226, 723–741. https://doi.org/10.1016/j.icarus.2013.06.027.

Farnocchia, D., Chesley, S.R., Vokrouhlick'y, D., Milani, A., Spoto, F., Bottke, W.F., 2013. Near Earth Asteroids with measurable Yarkovsky effect. Icarus 224, 1–13. https://doi.org/10.1016/j.icarus.2013.02.004.

Farnocchia, D., Chesley, S.R., Chamberlin, A.B., Tholen, D.J., 2015a. Star catalog position and proper motion corrections in asteroid astrometry. Icarus 245, 94–111. https://doi.org/10.1016/j.icarus.2014.07.033.31.

Farnocchia, D., Chesley, S.R., Milani, A., Gronchi, G.F., Chodas, P.W., 2015b. Long-Term Predictions, Impact Monitoring. In: Michel, Patrick, DeMeo, Francesca E., Bottke, William F. (Eds.), Asteroids IV. University of Arizona Press, Tucson, 978-0-816-53213-1, pp. 815–834. https://doi.org/10.2458/azuuapress9780816532131-ch041. 895 pp.

Farnocchia, D., Chesley, S.R., Micheli, M., 2015c. Systematic ranging and late warning asteroid impacts. Icarus 258, 18–27.

Farnocchia, D., Chesley, S.R., Chamberlin, A.B., 2016. Scout: orbit analysis and hazard assessment for NEOCP objects. In: AAS Division for Planetary Sciences Meeting Abstracts #48, 305.03.

Gaia Collaboration,Brown, A.G.A., Vallenari, A., Prusti, T., de Bruijne, J.H.J., Mignard, F., Drimmel, R., Babusiaux, C., Bailer-Jones, C.A.L., Bastian, U., et al., 2016. Gaia Data Release 1. Summary of the astrometric, photometric, and survey properties. Astron. Astrophys. 595 (A2). https://doi.org/10.1051/0004-6361/201629512.

Holsapple, K., Giblin, I., Housen, K., Nakamura, A., Ryan, E., 2002. Asteroid impacts: laboratory experiments and scaling. Laws 443–462.

Kim, S.-L., Lee, C.-U., Park, B.-G., et al., 2016. KMTNet: A network of 1.6 m wide-field optical telescopes installed at three Southern observatories. JKAS 49, 37.

Kizner, W., 1961. A method of describing miss distances for lunar and interplanetary trajectories. Planet. Space Sci. 7, 125–131. https://doi.org/10.1016/0032-0633(61)90293-8.

Landolt, A.U., 1992. UBVRI photometric standard stars in the magnitude range 11.5–16.0 around the celestial equator. Astron. J. 104, 340–371. https://doi.org/10.1086/116242.

Lawrence, K.J., Benner, L.A.M., Brozovic, M., Ostro, S.J., Jao, J.S., Giorgini, J.D., Slade, M.A., Jurgens, R.F., 2015. Goldstone radar imaging of near-Earth asteroid 2003 MS2. Icarus 260, 1–6. https://doi.org/10.1016/j.icarus.2015.06.001.

Mainzer, A., Grav, T., Bauer, J., Masiero, J., McMillan, R.S., Cutri, R.M., Walker, R., Wright, E., Eisenhardt, P., Tholen, D.J., Spahr, T., Jedicke, R., Denneau, L., De-Baun, E., Elsbury, D., Gautier, T., Gomillion, S., Hand, E., Mo, W., Watkins, J., Wilkins, A., Bryngelson, G.L., Del Pino Molina, A., Desai, S., G'omez Camus, M., Hidalgo, S.L., Konstantopoulos, I., Larsen, J.A., Maleszewski, C., Malkan, M.A., Mauduit, J.-C., Mullan, B.L., Olszewski, E.W., Pforr, J., Saro, A., Scotti, J.V., Wasserman, L.H., 2011. NEOWISE observations of near-Earth objects: preliminary results. Astrophys. J. 743, 156. https://doi.org/10.1088/0004-637X/743/2/156.

Mathias, D.L., Wheeler, L.F., Dotson, J.L., 2017. A probabilistic asteroid impact risk model: assessment of sub-300 m impacts. Icarus 289, 106–119. https://doi.org/10.1016/j.icarus.2017.02.009.

Micheli, M., Koschny, D., Drolshagen, G., Perozzi, E., Borgia, B., 2016. NEO followup, recovery and precovery campaigns at the ESA NEO Coordination Centre. In: Chesley, S.R., Morbidelli, A., Jedicke, R., Farnocchia, D. (Eds.), Asteroids: New Observations, New Models, Volume 318 of IAU Symposium, pp. 274–281. https://doi.org/10.1017/S1743921315009175.32.

Mommert, M., 2017. Photometrypipeline: an automated pipeline for calibrated photometry. Astron. Comput. 18, 47–53. https://doi.org/10.1016/j.ascom.2016.11.002.

Moskovitz, N.A., Abe, S., Pan, K.-S., Osip, D.J., Pefkou, D., Melita, M.D., Elias, M., Kitazato, K., Bus, S.J., DeMeo, F.E., Binzel, R.P., Abell, P.A., 2013. Rotational characterization of Hayabusa II target Asteroid (162173) 1999 JU3. Icarus 224, 24–31. https://doi.org/10.1016/j.icarus.2013.02.009.

MPEC 2012-T18, 2012. https://www.minorplanetcenter.net/mpec/K12/K12T18.html.

Naidu, S.P., Benner, L.A.M., Margot, J.-L., Busch, M.W., Taylor, P.A., 2016. Capabilities of Earth-based radar facilities for near-Earth asteroid observations. Astron. J. 152 (99). https://doi.org/10.3847/0004-6256/152/4/99.

Odden, C.E., Verhaegh, J.C., McCullough, D.G., Briggs, J.W., 2013. Lightcurve analysis for near-Earth asteroid 2012 TC4. Minor Planet Bull. 40, 176–177.

Ostro, S.J., Hudson, R.S., Benner, L.A.M., Giorgini, J.D., Magri, C., Margot, J.L., Nolan, M.C., 2002. Asteroid radar. Astronomy 151–168.

Polishook, D., 2013. Fast rotation of the NEA 2012 TC4 indicates a monolithic structure. Minor Planet Bull. 40, 42–43.

Rayner, J.T., Toomey, D.W., Onaka, P.M., Denault, A.J., Stahlberger, W.E., Vacca, W.D., Cushing, M.C., Wang, S., 2003. SpeX: A Medium-Resolution 0.8–5.5 Micron Spectrograph and Imager for the NASA Infrared Telescope Facility. 115. The Publications of the Astronomical Society of the Pacific, pp. 362–382. https://doi.org/10.1086/367745.

Rumpf, C.M., Lewis, H.G., Atkinson, P.M., 2017. Asteroid impact effects and their immediate hazards for human populations. Geophys. Res. Lett. 44, 3433–3440. https://doi.org/10.1002/2017GL073191.

Ryan, W., Ryan, E.V., 2017. Spin state of returning fly-by near earth asteroid 2012 TC4. In: AAS/Division for Planetary Sciences Meeting Abstracts #49, volume 49 of AAS/Division for Planetary Sciences Meeting Abstracts, page 204.06.

Scheeres, D.J., Benner, L.A.M., Ostro, S.J., Rossi, A., Marzari, F., Washabaugh, P., 2005. Abrupt alteration of Asteroid 2004 MN4's spin state during its 2029 Earth flyby. Icarus 178, 281–283. https://doi.org/10.1016/j.icarus.2005.06.002.

Scheeres, D.J., Britt, D., Carry, B., Holsapple, K.A., 2015. Asteroid Interiors and Morphology. pp. 745–766. https://doi.org/10.2458/azuuapress9780816532131-ch038.

Slade, M.A., Lee, C.G., Jao, J.S., Benner, L.A.M., Brozovic, M., Giorgini, J.D., Busch, M.W., 2010. First results of the New Goldstone Delay-Doppler radar chirp imaging system. In: AAS/Division for Planetary Sciences Meeting Abstracts #42, Volume 42 of Bulletin of the American Astronomical Society, pp. 1080.

Sonka, A.B., Gornea, A.I., Anghel, S., Birlan, M., 2017. Photometric observations of near Earth asteroid 2012 TC4. Rom. A. J. 27, 223–231.

Stokes, Grant H., et al., 2017. Update to determine the feasibility of enhancing the search and characterization of NEOs. Available online. National Aeronautics and Space Administration, Science Mission Directorate, Planetary Science Division, Washington D.C., pp. 216. https://www.nasa.gov/sites/default/files/atoms/files/2017_neo_sdt_

final_e-version.pdf.
Takahashi, Y., Busch, M.W., Scheeres, D.J., 2013. Spin state and moment of inertia characterization of 4179 Toutatis. Astron. J. 146, 95.
Tan, H., Gao, X., 2018. Lightcurve analysis for near-Earth asteroid 2012 TC4. The Minor Planet Bulletin (ISSN 1052-8091). Minor Planet Bull. 45 (3), 220–221.
Taylor, P.A., 3 colleagues, 2012. The shape and spin distributions of near-Earth asteroids observed with the Arecibo radar system. Bull. Am. Astron. Soc. 44 #302.07.
Tholen, D.J., 1984. Asteroid Taxonomy From Cluster Analysis of Photometry. PHD thesis. University of Arizona, Tucson (150p).
Vereš, P., Farnocchia, D., Chesley, S.R., Chamberlin, A.B., 2017. Statistical analysis of astrometric errors for the most productive asteroid surveys. Icarus 296, 139–149.
Virkki, A., Muinonen, K., Penttilä, A., 2014. Inferring asteroid surface properties from radar circular-polarization ratios. Meteorit. Planet. Sci. 49, 86–94.
Virkki, A., Markkanen, J., Tyynelä, J., Peltoniemi, J.I., Muinonen, K., 2015. Polarization by clusters of spherical particles at backscattering. Opt. Lett. 40, 3663–3666.
Vokrouhlický, D., Bottke, W.F., Chesley, S.R., Scheeres, D.J., Statler, T.S., 2015. The Yarkovsky and YORP effects. In: Michel, P. (Ed.), Asteroids IV. Univ. of Arizona, Tucson, pp. 509–531. https://doi.org/10.2458/azu_uapress_9780816532131-ch027.
Warner, B.D., 2013. Asteroid lightcurve analysis at the Palmer divide observatory: 2012 September–2013 January. Minor Planet Bull. 40, 71–80.
Warner, B.D., 2018. Near-Earth asteroid lightcurve analysis at CS3-Palmer divide station: 2017 July through October. Minor Planet Bull. 45, 19–34.
Wheeler, L.F., Register, P.J., Mathias, D.L., 2017. 2017. A fragment-cloud model for asteroid breakup and atmospheric energy deposition. Icarus 295, 149–169.